Cell Reports

Resource

A genome-wide library of MADM mice for single-cell genetic mosaic analysis

Graphical abstract

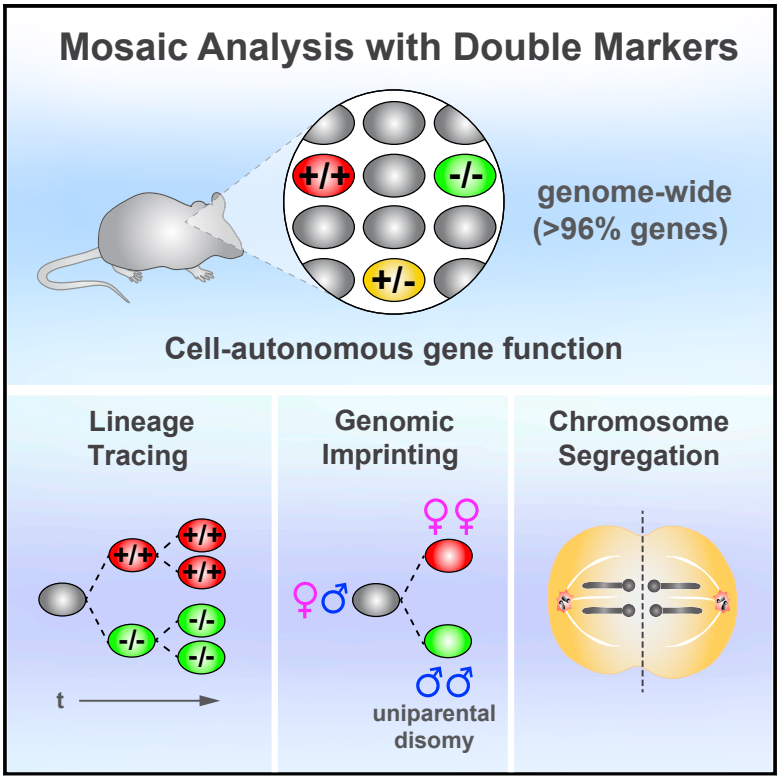

Authors

Ximena Contreras, Nicole Amberg, Amarbayasgalan Davaatseren, ..., Liqun Luo, Thomas Rülicke, Simon Hippenmeyer

Correspondence

simon.hippenmeyer@ist.ac.at

In brief

Contreras et al. generate a resource and suite of transgenic MADM mice for genetic mosaic analysis with double markers of >96% of the entire mouse genome. In addition to providing a proof of principle, they find non-random mitotic sister chromatid segregation in distinct somatic cell lineages *in vivo*.

Highlights

- Genome-wide resource for genetic mosaic analysis with double markers in mice
- Resource for dissection of cell-autonomous gene function of >96% of the mouse genome
- Resource for genome-wide analysis of genomic imprinting phenotypes
- MADM chromosomes reveal non-random mitotic sister chromatid segregation *in vivo*

Contreras et al., 2021, Cell Reports *35*, 109274
June 22, 2021 © 2021 The Author(s).
https://doi.org/10.1016/j.celrep.2021.109274

CellPress

Cell Reports

CellPress
OPEN ACCESS

Resource

A genome-wide library of MADM mice for single-cell genetic mosaic analysis

Ximena Contreras,[1] Nicole Amberg,[1] Amarbayasgalan Davaatseren,[1] Andi H. Hansen,[1] Johanna Sonntag,[1] Lill Andersen,[2] Tina Bernthaler,[2] Carmen Streicher,[1] Anna Heger,[1] Randy L. Johnson,[3] Lindsay A. Schwarz,[4,5] Liqun Luo,[4] Thomas Rülicke,[2] and Simon Hippenmeyer[1,6,*]

[1]Institute of Science and Technology Austria, Am Campus 1, 3400 Klosterneuburg, Austria
[2]Institute of Laboratory Animal Science, University of Veterinary Medicine Vienna, 1210 Vienna, Austria
[3]Department of Biochemistry and Molecular Biology, University of Texas, Houston, TX 77030, USA
[4]HHMI and Department of Biology, Stanford University, Stanford, CA 94305, USA
[5]Present address: St. Jude Children's Research Hospital, Memphis, TN 38105, USA
[6]Lead contact
*Correspondence: simon.hippenmeyer@ist.ac.at
https://doi.org/10.1016/j.celrep.2021.109274

SUMMARY

Mosaic analysis with double markers (MADM) offers one approach to visualize and concomitantly manipulate genetically defined cells in mice with single-cell resolution. MADM applications include the analysis of lineage, single-cell morphology and physiology, genomic imprinting phenotypes, and dissection of cell-autonomous gene functions *in vivo* in health and disease. Yet, MADM can only be applied to <25% of all mouse genes on select chromosomes to date. To overcome this limitation, we generate transgenic mice with knocked-in MADM cassettes near the centromeres of all 19 autosomes and validate their use across organs. With this resource, >96% of the entire mouse genome can now be subjected to single-cell genetic mosaic analysis. Beyond a proof of principle, we apply our MADM library to systematically trace sister chromatid segregation in distinct mitotic cell lineages. We find striking chromosome-specific biases in segregation patterns, reflecting a putative mechanism for the asymmetric segregation of genetic determinants in somatic stem cell division.

INTRODUCTION

Genetic mosaic individuals contain cells of distinct genotypes. The phenomenon of genetic mosaicism occurs naturally and is widespread across multicellular organisms. Mosaicism may progressively emerge during life but remain silent with no obvious phenotypes (Yizhak et al., 2019). However, mosaicism is also associated with pathologies in humans including cancer or many neurological disorders (Biesecker and Spinner 2013; D'Gama and Walsh 2018). Genetic mosaic animals have been experimentally created in a number of species, and mosaic analyses provided fundamental insights in a variety of biological systems (Xu and Rubin 1993; Rossant and Spence 1998; Lee and Luo 1999, 2001; Yochem and Herman 2003; Zugates and Lee 2004; Zong et al., 2005; Lozano and Behringer 2007; Luo 2007; Germani et al., 2018; Kim et al., 2019).

One powerful application inherent to induced genetic mosaics is the ability to alter gene function at a high spatiotemporal resolution. A certain tissue can contain homozygous mutant cells for a gene of interest and wild-type cells whose phenotypes can be compared with each other directly. If the genetic mosaic is sparse, even essential genes can be manipulated without affecting the overall health or viability of the animal. Furthermore, sparse genetic mosaics provide a highly effective means with which to study the causal relationship of genetic alteration and phenotypic manifestation at the individual cell level. Genetic mosaics also facilitate the analysis of cell competition and provide an assay to create models of disease. Genetic mosaics have been most extensively generated in the fruit fly by capitalizing upon mitotic recombination between homologous chromosomes (Morgan and Bridges 1919; Stern 1936; Hotta and Benzer 1970; Xu and Rubin 1993; Lee and Luo 1999, 2001; Zugates and Lee 2004). Although technically slightly more challenging, the generation of genetic mosaics in mice is becoming routine. A number of experimental approaches have been established including mosaic analysis with double markers (MADM) that is also based on mitotic recombination (Zong et al., 2005; Luo 2007; Tasic et al., 2012; Hippenmeyer 2013).

MADM relies on Cre/*loxP*-mediated interchromosomal recombination to simultaneously generate homozygous mutant cells for a candidate gene of interest and wild-type cells in an otherwise heterozygous background. The induction of genetic mosaicism can be spatiotemporally controlled by the use of cell-type-specific Cre/ER driver lines (Zong et al., 2005; Hippenmeyer et al., 2013; Ali et al., 2014; Beattie et al., 2020). Concurrent to the generation of genetic mosaicism, two split genes, encoding green fluorescent protein (GFP) and tdTomato (tdT) fluorescent markers, are reconstituted that permit unequivocal tracing of individual cellular phenotypes in the homozygous mutant and heterozygous and wild-type cells, with each labeled

This is an open access article under the CC BY-NC-ND license (http://creativecommons.org/licenses/by-nc-nd/4.0/).

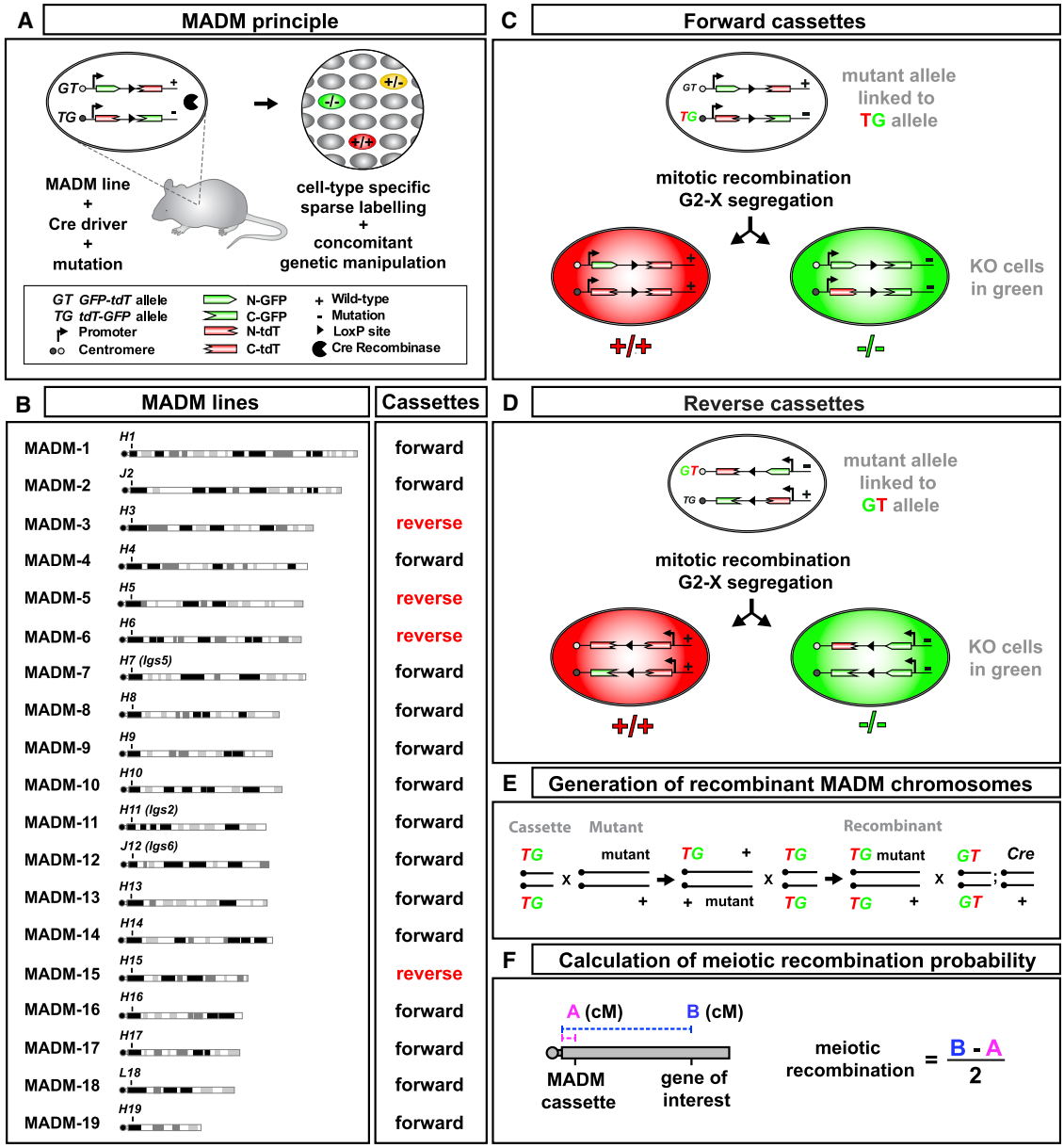

Figure 1. Extension of MADM to all 19 mouse autosomes

(A) Summary of the MADM principle. For MADM, two chimeric split marker genes containing partial coding sequences of EGFP and tdT are inserted into identical genomic loci of homologous chromosomes. Following Cre-recombinase-mediated interchromosomal (trans) recombination during mitosis, the split marker genes are reconstituted and functional green and red fluorescent proteins expressed. As a result, green GFP$^+$, red tdT$^+$, and yellow GFP$^+$/tdT$^+$ cells appear sparsely, due to an inherently low stochastic interchromosomal recombination rate, within the genetically defined cell population expressing Cre recombinase. Introduction of a mutant allele distal to the MADM cassette results in a genetic mosaic with homozygous mutant cells labeled in one color (e.g., green GFP$^+$) and homozygous wild-type sibling cells in the other (e.g., red tdT$^+$). Heterozygous cells appear in yellow (GFP$^+$/tdT$^+$).

(B) Expansion of MADM to all mouse autosomes. Transgenic mice with MADM cassettes inserted close to the centromere have been generated for all 19 mouse autosomes. The directionality (forward, centromere-telomere; reverse, telomere-centromere) of marker gene transcription is indicated.

(C) MADM labeling scheme for cassettes inserted in forward direction. MADM experiments involving forward cassettes require that the mutant allele of a candidate gene must be linked to the T-G MADM cassette in order for mutant cells to be labeled in green upon a G2-X MADM event.

(D) MADM labeling scheme for cassettes inserted in reverse direction. MADM experiments involving reverse cassettes require that the mutant allele of a candidate gene must be linked to the G-T MADM cassette in order for mutant cells to be labeled in green upon a G2-X MADM event.

(E) Generation of recombinant MADM chromosomes. To genetically link a mutant allele of a candidate gene of interest to the corresponding chromosome containing the T-G MADM cassette (i.e., forward orientation), it is necessary to first cross mice bearing the T-G MADM cassette with mice bearing the mutant allele. Resulting F1 transheterozygous offspring are then backcrossed to mice homozygous for the T-G MADM cassette. In F2, recombinant offspring emerge from meiotic recombination events in the germline. These F2 recombinants now contain both the MADM cassette (in homozygous configuration) and the mutant

(legend continued on next page)

in distinct colors with 100% accuracy (Zong et al., 2005; Hippenmeyer et al., 2010; Figure 1A; Figure S1).

The MADM approach enables unparalleled lineage tracing, and MADM-labeled cells can be assessed by histological means, physiological analysis, and optical imaging *in vivo* (Espinosa et al., 2009; Hippenmeyer et al., 2010; Liang et al., 2013; Gao et al., 2014; Joo et al., 2014; Riccio et al., 2016; Beattie et al., 2017; Henderson et al., 2019; Lv et al., 2019; Ortiz-Álvarez et al., 2019).

MADM technology represents one approach to probe genomic imprinting and the function of imprinted genes (Hippenmeyer et al., 2013; Laukoter et al., 2020b). MADM can be applied to create uniparental chromosome disomy (UPD; somatic cells with two copies of either the maternal or paternal chromosome) and visualize imprinting effects at morphological and transcriptional levels with single-cell resolution (Hippenmeyer et al., 2013; Laukoter et al., 2020a, 2020c).

One clinically relevant application of MADM is the tracing of tumor growth upon sparse or clonal ablation of tumor suppressor genes and/or to assay for the effects of therapeutic agents. As such, MADM has been used for the analysis of tumor formation and the delineation of cancer cell of origin at the single-cell level in the brain and distinct organs (Muzumdar et al., 2007, 2016; Liu et al., 2011; Gonzalez et al., 2018; Tian et al., 2020; Yao et al., 2020).

A current limitation of the MADM technology is that it can only be applied to study candidate genes located on chromosome 7 (chr7), chr11, and chr12 and distal to the *Rosa26* locus on chr6, where MADM cassettes have been introduced (Zong et al., 2005; Hippenmeyer et al., 2010, 2013). Thus, less than 25% of all genes in the mouse genome can be subjected to MADM analysis as described above. Here, we overcome this constraint and expand MADM technology to all mouse autosomes. We provide validation of all MADM reporters and quantitative assessment of the efficacy of MADM labeling in a variety of organs and tissues and a number of clinically relevant stem cell niches across the entire mouse. Furthermore, we use engineered MADM chromosomes to systematically determine sister chromatid segregation patterns in several somatic cell lineages. Our analysis revealed that sister chromatid segregation patterns in mitotic progenitor cell divisions are highly biased in a chromosome-specific manner and are further affected by cell type *in vivo*.

RESULTS

Expansion of MADM to all mouse autosomes

For MADM, two reciprocally chimeric marker genes need to be targeted to identical loci on homologous chromosomes (Zong et al., 2005). The chimeric marker genes (*GT* and *TG* alleles) consist of N- or C-terminal halves of the coding sequences for GFP (enhanced GFP) and red fluorescent protein (tdT) interspersed by an intron with the *loxP* site (Hippenmeyer et al., 2010; Figure 1A; Figure S1). Here, we expanded MADM to all 19 mouse autosomes with the goal to enable MADM for the vast majority, nearly genome-wide, of autosomal genes in the mouse genome. Mouse autosomes consist of only one chromosome arm (i.e., telocentric conformation). We thus rationalized that inserting the MADM cassettes as close as possible to the centromere would maximize the number of genes located distally to the MADM cassette insertion site for prospective MADM experiments (Hippenmeyer et al., 2010, 2013; Figures 1A and 1B).

To identify suitable sites for MADM cassette targeting, we applied a number of key criteria. The loci should (1) locate to intergenic regions to minimize the probability of disrupting endogenous gene function and (2) permit spatially and temporally ubiquitous and biallelic expression of the reconstituted GFP and tdT markers. To fulfill the first criteria, we mapped gene by gene the genetic landscape of the centromeric-most 20 Mbp of all autosomes using the UCSC Genome Browser (https://www.genome.ucsc.edu; GRCm38/mm10). Next, we assessed EST (expression sequence tag) expression patterns of the neighboring genes flanking the putative targeting sites and serving as proxy for the spatiotemporal extent of transgene expression. The final choice of the prime targeting loci (Figure 1B; Figures S2 and S3; Table S1) was based upon the most ideal combination of the above key criteria. In total, more than 20,000 protein-coding genes, corresponding to >96% of the entire annotated mouse genome (GRCm38/mm10), are located distally to the MADM targeting loci across all 19 autosomes (Table S1).

Next, we cloned the selected genomic targeting loci and inserted the MADM cassettes (Hippenmeyer et al., 2010) by homologous recombination in mouse embryonic stem cells (ESCs) (Figure S4; see STAR Methods for details). MADM cassettes were inserted in a centromere-to-telomere transcriptional direction (Figure 1B, forward) except for chr3, chr5, chr6, and chr15, which required opposite directionality (Figure 1B, reverse) in order to best fulfill our locus choice criteria. The directionality of reconstituted MADM marker gene transcription, upon interchromosomal recombination, has consequences for the coupling of mutant and wild-type genotypes with fluorescent labeling upon mitosis (Figures 1C and 1D). In order to genetically link a mutant allele of a candidate gene to the corresponding chromosome containing the MADM cassette, meiotic recombination in the germline can be used (e.g., Hippenmeyer et al., 2010; Laukoter et al., 2020b; (Figures 1E and 1F). The probability for meiotic recombination that results in the linkage of the mutant allele with the MADM cassette can be estimated (Figure 1F) once the location (cM) of the mutant allele (genomic locus) has been determined by using, for example, the Mouse Genome Informatics (MGI) database (https://www.informatics.jax.org).

Homologous recombination frequencies in ESCs were relatively high for all selected loci (for some, >50%), hinting at an open chromatin structure that should be an advantage for

allele linked on the same chromosome. For experimental MADM mice, F2 recombinants are crossed with mice bearing the G-T MADM cassette and a Cre driver of interest.

(F) Calculation of predicted meiotic recombination frequency. The probability for meiotic recombination resulting in the linkage of the MADM cassette with the mutant allele can be estimated by the genetic distance of the MADM cassette to the location of the mutant allele divided by two.

See also Figures S1–S4 and Table S1.

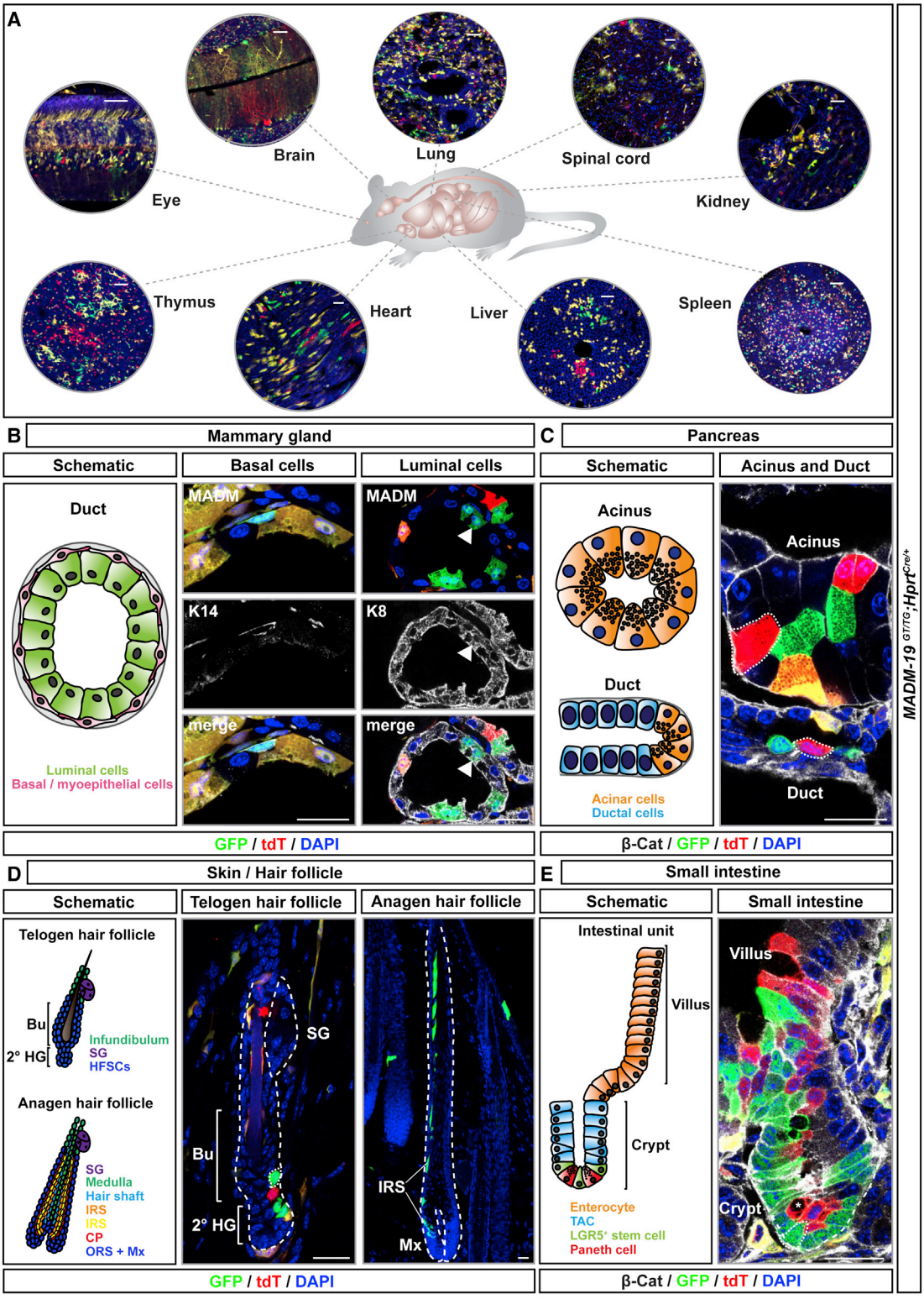

Figure 2. MADM labeling pattern in different organs and stem cell niches

(A) Overview of MADM labeling (green, GFP; red, tdT; yellow, GFP/tdT) in *MADM-19*$^{GT/TG}$ in combination with *Hprt*-Cre at P21. Diverse tissues/organs including eye, brain, lung, spinal cord, kidney, spleen, liver, heart, and thymus are illustrated.

(legend continued on next page)

prospective mitotic Cre-mediated interchromosomal recombination. Next, chimeric founder mice were generated by blastocyst injection. Homozygous *MADM*$^{GT/GT}$ and *MADM*$^{TG/TG}$ stock lines were established upon successful germline transmission of the respective MADM cassettes (Figure S4) by using specific genotyping primers (Table S2).

Ubiquitous labeling in all MADM reporter lines across different organs

We systematically analyzed the MADM labeling pattern upon Cre-mediated interchromosmal recombination in all MADM lines (Figure S4E). First, we crossed all *MADM*$^{GT/GT}$ lines to mice that carry the Cre transgene within the X-linked *Hprt* (encoding hypoxanthine guanine phosphoribosyl transferase) genomic locus. The *Hprt*-Cre driver is spatiotemporally ubiquitously and constitutively expressed (Tang et al., 2002). In female mice, inactivation of the X chromosome results in mosaic *Cre* expression from the *Hprt* locus and thus highly variable MADM labeling patterns (Zong et al., 2005; Hippenmeyer et al., 2013). We therefore analyzed male experimental MADM (*MADM*$^{GT/TG}$;*Hprt*$^{Cre/Y}$) animals for a first pass comparative assessment. We detected MADM labeling in all organs analyzed—including brain, spinal cord, eye, heart, lung, liver, kidney, thymus, and spleen (Figure 2A)—and in all MADM lines. The relative recombination frequency, at least at this superficial qualitative level, appeared to correlate in distinct selected organs across all 19 MADM lines (Figures 2 and S5–S9).

MADM labeling in clinically relevant adult stem cell niches

We next evaluated a number of stem cell niches with high clinical relevance. Because it is important to know the approximate scale of labeling for determining sample size in a MADM experiment, we chose two different MADM models in combination with *Hprt*-Cre driver for these analyses, as follows: MADM-19 that shows relatively dense MADM labeling and MADM-4 that represents one of the sparsest MADM.

First, we focused on the mammary gland (Figure 2B), the site where breast cancer initiates. The mammary gland harbors two types of unipotent stem cell lineages, namely, the K14$^+$ myoepithelial (or basal) cells and the K8$^+$ luminal cells (Van Keymeulen et al., 2011). Myoepithelial and luminal stem cell populations are derived from a multipotent progenitor during embryonic development (Wuidart et al., 2018), become unipotent at birth, and can both give rise to mammary tumors upon transformation. We evaluated the MADM-labeling pattern in the postnatal mammary gland in adult lactating 4-month-old female *MADM-19*$^{GT/TG}$;*Hprt*$^{Cre/+}$ (Figure 2B) and *MADM-4*$^{GT/TG}$;*Hprt*$^{Cre/+}$ (Figure S7A) mice and could readily detect GFP$^+$ (green), tdT$^+$ (red), and GFP$^+$/tdT$^+$ (yellow) cells in both K14$^+$ basal and K8$^+$ luminal cells.

Next, we analyzed pancreatic epithelial cells that can be divided into secretory acinar cells and ductal epithelial cells. Although the tumor cell of origin for pancreatic cancer remains controversial, oncogenic drivers can trigger pancreatic ductal adenocarcinoma (PDAC) from both ductal and acinar cells (Ferreira et al., 2017; Lee et al., 2019). In both, *MADM-19*$^{GT/TG}$;*Hprt*$^{Cre/+}$ and *MADM-4*$^{GT/TG}$;*Hprt*$^{Cre/+}$ mice at postnatal day 21 (P21), we noticed MADM-labeled cells in the acinus and duct within the pancreas (Figure 2C and S7B).

Hair follicles are a prime stem cell model for the study of tissue regeneration but also for skin cancer including melanoma (Sun et al., 2019). Hair follicles are appendages of the epidermal lineage and undergo cycling rounds of stem cell activation in order to generate new hair (Fuchs and Nowak 2008). The stem cells are located in the secondary hair germ (2° HG) and lower part of the bulge (Bu) of a resting follicle (telogen follicle) (Figure 2D). They become activated, start to proliferate, and expand the hair follicle deep down into the dermis. Progenitors located at the bottom of the activated follicle (anagen follicle) form the matrix, from where epithelial hair lineages are specified (Hsu et al., 2014). Such differentiated hair lineages comprise the companion layer (CP), distinct layers of inner root sheath (IRS), and cuticle and cortex of the hair shaft (HS), as well as the innermost hair layer the medulla (Me). Once hair regeneration is completed, the follicles undergo a destructive phase (catagen) and enter the quiescent resting phase again. In the skin of *MADM-19*$^{GT/TG}$;*Hprt*$^{Cre/+}$ and *MADM-4*$^{GT/TG}$;*Hprt*$^{Cre/+}$ mice, we observed prominent MADM labeling in all compartments of the hair follicle and importantly in the hair follicle stem cells (Figures 2D and S7C).

Next, we analyzed MADM labeling in the small intestine that represents another critical model for the study of stem-cell-mediated regeneration but also intestinal cancer (Barker et al., 2009). Intestinal stem cells replenishing the epithelium are LGR5$^+$ and located in the crypt base (Barker et al., 2007). They are intermingled with secretory Paneth cells and divide constantly in order to rejuvenate the epithelial cell layer on the villus surface. Interestingly, LGR5$^+$ stem cells mostly divide symmetrically and undergo neutral competition within the crypt, thus driving the crypt toward monoclonality (Snippert et al., 2010). In order to evaluate the potential for MADM-based lineage tracing, the study of loss of gene function, and analysis of stem

(B) Schematic (left) and MADM labeling (middle/right; green, GFP; red, tdT; yellow, GFP/tdT) in mammary gland of lactating *MADM-19*$^{GT/TG}$;*Hprt*$^{Cre/+}$ female at 4 months of age. Basal/myoepithelial (middle) and luminal (right) cells are stained with antibodies against K14 and K8 (white), respectively.
(C) Schematic (left) MADM labeling (right; green, GFP; red, tdT; yellow, GFP/tdT) in *MADM-19*$^{GT/TG}$;*Hprt*$^{Cre/+}$ pancreas, acinus, and duct, at P21. Epithelial cells are visualized by antibody staining against β-catenin (white; β-Cat). Acinar cells are identified by the presence of intracellular secretory granules.
(D) Schematic (left) and MADM labeling (middle/right; green, GFP; red, tdT; yellow, GFP/tdT) in telogen (middle) and anagen (right) hair follicles in *MADM-19*$^{GT/TG}$;*Hprt*$^{Cre/+}$ at P21 (telogen) and P28 (anagen). Bu, bulge; 2° HG, secondary hair germ; SG, sebaceous gland; IRS, inner root sheath; CP, companion layer; ORS, outer root sheath; Mx, matrix.
(E) Schematic (left) and MADM labeling (right; green, GFP; red, tdT; yellow, GFP/tdT) in small intestine in *MADM-19*$^{GT/TG}$;*Hprt*$^{Cre/+}$ at P21. Epithelial cells are visualized by antibody staining against β-catenin (white; β-Cat). Asterisk marks a Paneth cell, identified by the presence of intracellular granules. TAC, transit-amplifying cell; LGR5, leucine-rich repeat-containing G-protein coupled receptor 5.
Nuclei were stained using DAPI. Scale bar: 50 μm (A) and 20 μm (B–E).
See also Figures S5–S8.

cell behavior in the intestinal crypts, we dissected the intestine of *MADM-19*$^{GT/TG}$;*Hprt*$^{Cre/+}$ and *MADM-4*$^{GT/TG}$;*Hprt*$^{Cre/+}$ mice at P21. We observed MADM-labeled cells in all compartments of the intestinal unit, including the villus and the crypt (Figure 2E and S7D).

Lastly, we validated one of the MADM reporters in a disease-relevant setting. We used MADM-18 lines to examine the effect of clonal loss of *Apc* (*adenomatous polyposis coli*). APC functions as a tumor suppressor and mutations in *APC* cause hereditary and sporadic human bowel cancers upon loss of heterozygosity (Behrens et al., 1998; Fodde et al., 2001). To mimic the intestinal tumor initiation, we generated genetic mosaic mice harboring green *Apc*$^{-/-}$ cells by using an *Apc*-flox allele (Cheung et al., 2010) and red wild-type cells in an otherwise heterozygous environment (Figure 3). At 3 months of age, *MADM-18*$^{GT/TG}$;*Hprt*$^{Cre/+}$ control mice showed several red- or green-labeled normal crypt-villus units (Figures 3A–3D). Note that MADM labeling within crypt-villus units appeared exclusively unicolor, reflecting monoclonality due to stochastic competition between dividing intestinal stem cells (Snippert et al., 2010). In contrast, all *MADM-18*$^{GT/TG,Apc}$;*Hprt*$^{Cre/+}$ experimental mice, in which *Apc*$^{-/-}$ cells are labeled in green and *Apc*$^{+/+}$ cells in red by design, displayed one or several green-labeled cancerous lesions (adenomas), derived from *Apc*$^{-/-}$ stem cells, in their small intestine and colon (Figures 3E–3G; Barker et al., 2009). Yet, we did not detect any tumors derived from red control cells in *MADM-18*$^{GT/TG,Apc}$;*Hprt*$^{Cre/+}$ experimental mice (Figure 3D). Antibody staining against phosphohistone H3 (P-H3) confirmed that normal crypt-villus units display proliferation only within the crypt compartment but not within the villus epithelium (Figures 3B, 3C, and 3F). In contrast, adenomas derived from green *Apc*$^{-/-}$ cells in mosaic mice contained proliferating tumor cells in regions outside the crypt compartment (Figure 3F) as previously reported (Schepers et al., 2012). In summary, we validated one of the MADM lines for functional genetic mosaic analysis in the context of the *Apc* model (Figures 3H and 3I) for tumor initiation and growth.

Genomic imprinting phenotypes in liver cells with UPD

MADM can create UPD (Figure 4A) to analyze imprinting phenotypes at the single-cell level that result from the imbalanced expression of imprinted genes (Hippenmeyer et al., 2013; Laukoter et al., 2020b, 2020c; Pauler et al., 2021). Prominent imprinting phenotypes have been observed in the liver where, for instance cells with MADM-induced paternal UPD of chr7 exhibit overgrowth (Hippenmeyer et al., 2013), in accordance with the kinship hypothesis that stipulates a major growth regulatory function of genomic imprinting (Haig 2004; Tucci et al., 2019). Because imprinted genes are located throughout the genome, we analyzed the liver in all 19 MADM reporters in combination with *Hprt*-Cre (Figures 4B–4U) for potential imprinting phenotypes. We readily observed the growth advantage of hepatocytes with paternal UPD of chr7 (Figures 4H and 4V) but also noticed that cells with paternal UPD of chr11 (Figures 4L and 4V) and chr17 (Figures 4R and 4V) showed significant over-representation in comparison to cells with maternal UPD. The maternally expressed growth inhibitory imprinted genes *Grb10* and *Igf2r* are located on chr11 and chr17, respectively. Thus, although overexpression of growth-promoting *Igf2* in UPD of chr7 leads to paternal growth dominance (Hippenmeyer et al., 2013), the absence of growth-antagonizing *Grb10* or *Igf2r* (Smith et al., 2006) may result in the growth advantage of cells with paternal UPD of chr11 or chr17. We did not find significant UPD-mediated phenotypes in the liver of any other MADM (Figures 4B–4U).

Quantification of recombination efficiency of all MADM chromosomes

To systematically determine recombination frequencies comparatively in all MADMs, we quantified the absolute density of MADM-labeled neurons in the neocortex of P21 mice by using the *Emx1*-Cre driver (Figures 5A, 5B, and S9). We first assessed MADM labeling originating from G2-X events and quantified the numbers of green GFP$^+$ and red tdT$^+$ projection neurons per cubic millimeter (Figures 5A and 5B). The relative number of red tdT$^+$ versus green GFP$^+$ projection neurons was not significantly different across MADM lines (Figures 5B; Table S3). We classified the MADM reporters into three categories, as follows: (1) sparse (<25 cells/mm^3), (2) intermediate (25–100 cells/mm^3), and (3) dense (>100 cells/mm^3). Because all MADM-targeting loci have been selected by using the same criteria, the origin of the variability in recombination frequency across all MADMs is currently not clear. In mice, the pairing of homologous chromosomes in somatic cells is infrequent and under tight regulation, unlike in the fruit fly *Drosophila* (Apte and Meller 2012). Thus, the individual dynamic organization of different homologous chromosomes within the nucleus may result in distinct probabilities of Cre-mediated interchromosomal recombination. It is also important to mention that insertion of the MADM cassettes at more distal locations in the same chromosome could lead to a distinct recombination probability. In any case, all MADM reporters do work as predicted from the MADM principle (Figures 1 and S1) in all organs analyzed (Figures 2, 3, 4, 5, and S5–S9). Importantly, even the sparsest MADM lines (including MADM-4 [Hansen and Hippenmeyer, unpublished observation] and MADM-6 [Takeo et al., 2021]) reliably permit functional genetic mosaic analysis of candidate genes.

MADM reveals chromosome-specific biases in mitotic sister chromatid segregation patterns

Previous *in vitro* studies have used mitotic recombination in ESCs to monitor the randomness of sister chromatid segregation patterns upon mitosis (Liu et al., 2002; Armakolas and Klar 2006). Against common belief, initial results indicated that sister chromatids derived from a homologous pair of chromosomes did not segregate randomly to daughter cells. Instead, G2-X segregation (two recombinant chromosomes segregate away from each other), thus reflecting one particular pattern of sister chromatid segregation, prevailed in ESCs for chr7 (Liu et al., 2002). Furthermore, ESC-derived endoderm cell lines exhibited complete bias toward G2-X (Armakolas and Klar 2006). Conversely, ESC-derived neuroectoderm cell lines never showed G2-X (Armakolas and Klar 2006). Although these results indicated that cell type may influence the selective segregation of sister chromatids, such a hypothesis is based on the analysis of only one chromosome and has not been examined in the context of intact

CellPress
OPEN ACCESS

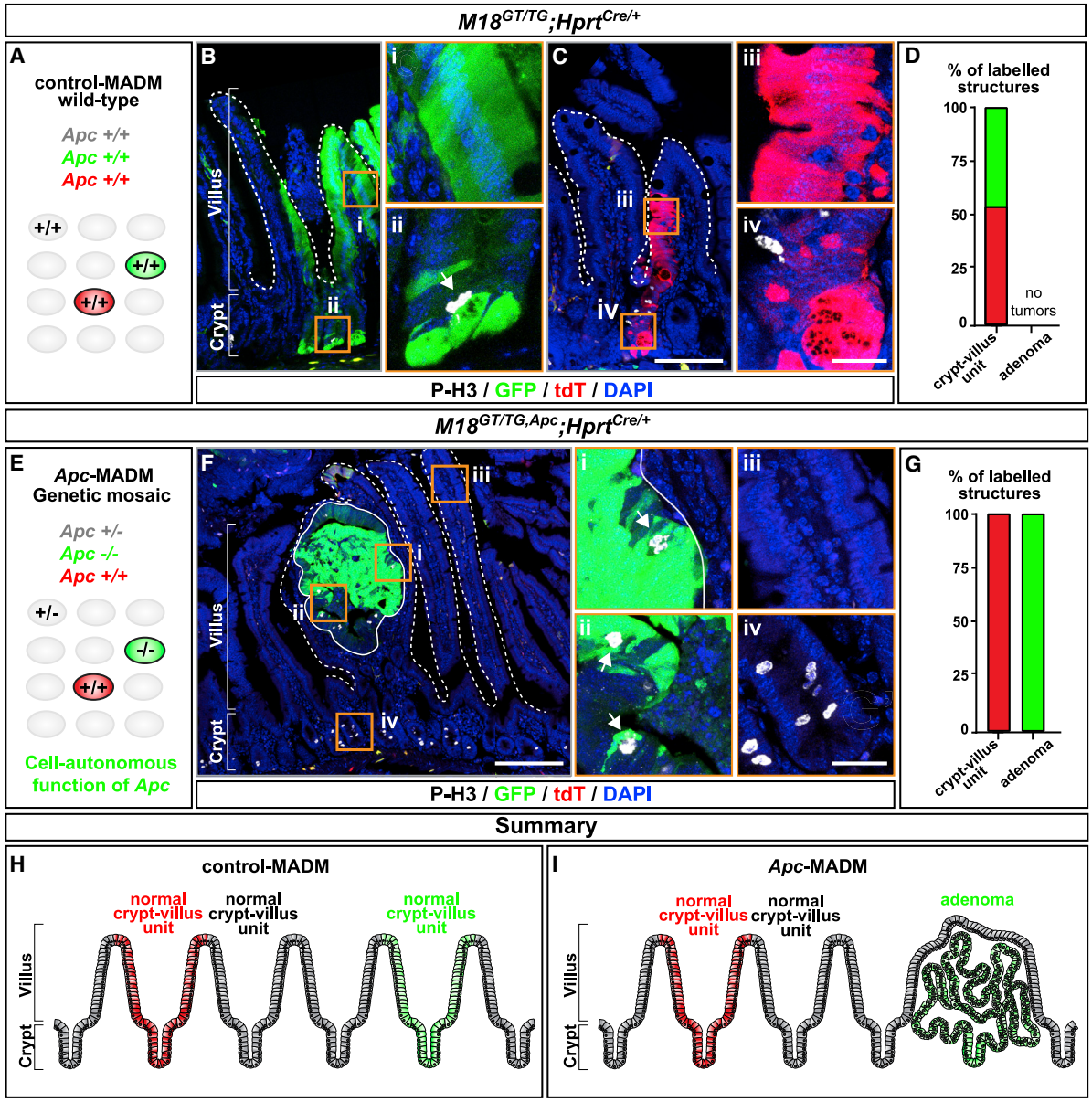

Figure 3. *Apc*-tumor model at single-cell resolution using the MADM-18 line

(A) Schematic representation of MADM labeling (green, GFP; red, tdT) and respective cellular genotypes in wild-type *MADM-18*$^{GT/TG}$;*Hprt*$^{Cre/+}$ mice.

(B and C) P-H3 staining (white) in small intestine in *MADM-18*$^{GT/TG}$;*Hprt*$^{Cre/+}$ mice at 3 months of age. (B) Overview of unicolor (monoclonal) green wild-type crypt-villus units with insets highlighting non-proliferative villus epithelium (i) and a proliferative cell within the crypt (white arrow) (ii); (C) overview and unicolor (monoclonal) red wild-type crypt-villus units with insets highlighting non-proliferative villus epithelium (iii) and a proliferating cell within the crypt (iv).

(D) Quantification of the percentage of intestinal structures displaying MADM labeling. Data obtained from n = 3 male *MADM-18*$^{GT/TG}$;*Hprt*$^{Cre/+}$ mice at 3 months of age.

(E) Schematic representation of MADM labeling (green, GFP; red, tdT) and respective cellular genotypes in genetic mosaic *MADM-18*$^{GT/TG,Apc}$;*Hprt*$^{Cre/+}$ mice.

(F) P-H3 staining (white) in small intestine in male *MADM-18*$^{GT/TG,Apc}$;*Hprt*$^{Cre/+}$ mice at 3 months of age with insets highlighting a proliferating adenoma cell at the boundary to the non-proliferative villus epithelium (white arrow) (i), proliferating adenoma cells within the tumor (white arrows) (ii), non-proliferative normal villus epithelium (iii), and proliferative cells within a normal crypt compartment (iv).

(G) Quantification of the percentage of intestinal structures displaying MADM labeling. Green *Apc*$^{-/-}$ cells display 100% transformation and tumor initiation, whereas red wild-type cells solely give rise to normal crypt-villus-units. Data obtained from n = 3 male *MADM-18*$^{GT/TG,Apc}$;*Hprt*$^{Cre/+}$ mice at 3 months of age.

(H and I) Summary of MADM labeling in small intestine of control *MADM-18*$^{GT/TG}$;*Hprt*$^{Cre/+}$ (H) and genetic mosaic *MADM-18*$^{GT/TG,Apc}$;*Hprt*$^{Cre/+}$ mice (I). Note that in the mosaic, red wild-type cells give rise to normal crypt-villus units and green *Apc*$^{-/-}$ cells initiate tumor development and subepithelial invasion of adenomas. Nuclei were stained using DAPI. Scale bar: 100 μm (B, C, and F) and 25 μm (i–iv).

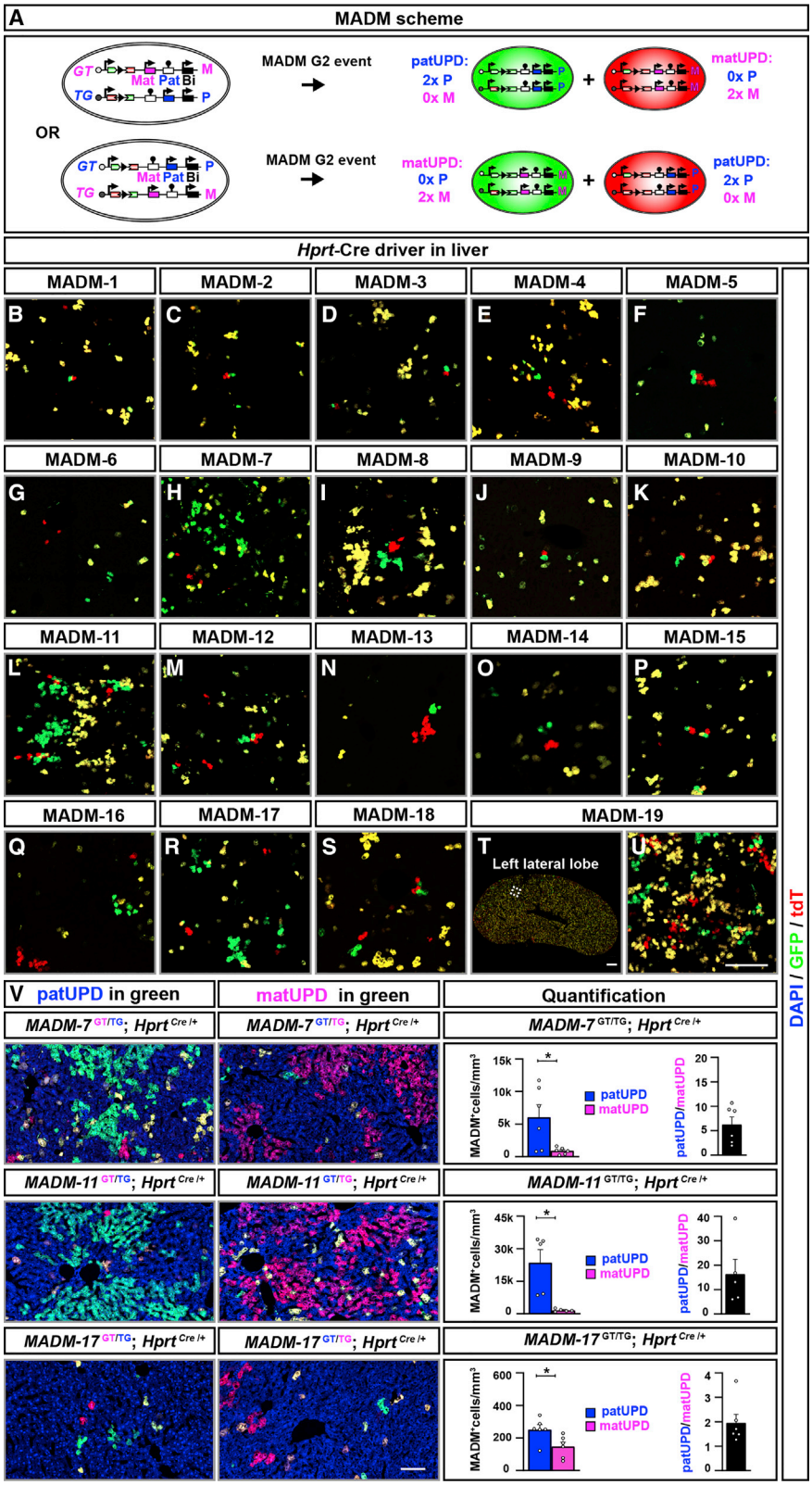

(legend on next page)

tissue. To this end, we used the entire library of MADM-rendered homologous chromosomes to systematically trace sister chromatid segregation patterns of all 19 mouse autosomes in a number of somatic cell lineages *in vivo*.

We exploited the inimitable feature provided by the MADM principle (Figures 5C and S1)—the differential fluorescent labeling of pairs of nascent sister cells upon mitosis that is dependent on how recombinant chromosomes segregate during cell division. G2-X segregation of recombinant MADM chromosomes can be unambiguously identified by the presence of red and green cells. However, G2-Z segregation, producing yellow cells, cannot be identified without ambiguity because G1 and/or postmitotic G_0 events also result in yellow cells (Zong et al., 2005; Figures 5C and S1). Therefore, we capitalized upon the power of unequivocal G2-X identification—but also taking into consideration the caveat of yellow cells potentially reflecting a mix of G2-Z and G1/G_0—and defined "yellow-green-red-index" (YGRI) as a proxy for sister chromatid segregation patterns (Figure 5D).

First, we systematically determined the YGRI of pyramidal projection neurons in the P21 neocortex for all 19 MADM reporters in combination with the *Emx1*-Cre driver (expressed in cortical progenitor cells and thereby limiting G_0 events) (Figure 5E; Table S3). Contrary to the prediction and expectation based on cell culture data (no G2-X in neuroectodermal lineage [Armakolas and Klar 2006]), we always observed G2-X events. Interestingly, the YGRI values ranged from ~1 for MADM-2 and MADM-17 to ~10 for MADM-15 (Figure 5E, top). The values of the YGRI did not correlate with the sizes of the respective MADM chromosomes. Next, we compared the values of the YGRI with the absolute recombination frequencies (RFI, recombination frequency index), i.e., density of G2-X MADM labeling as indicated in Figure 5B. In the ranking plot in which the axes indicate YGRI versus RFI, there was no apparent correlation (Figure 5E, bottom) of YGRI with RFI. In summary, we detected highly distinct YGRI for different MADM chromosomes, suggesting distinct sister chromatid segregation patterns in the cortical *Emx1*$^+$ projection neuron lineage.

Previous studies implicated left-right dynein (LRD)—the only protein thus far in a mammalian cell culture system—in the selective sister chromatid segregation process (Armakolas and Klar 2007). Intriguingly, mutations in the gene (*Dnah11*) encoding LRD causes randomization of left-right laterality in mice (half of the animals develop with mirror-imaged visceral organs) (Hummel and Chapman 1959; Supp et al., 1997). Based on the above findings from cell culture, we next assessed whether *Dnah11* could play a role in biased chromosome-specific sister chromatid *in vivo* as well. We crossed the MADM system to *iv* (*situs inversus*) (a spontaneous mutation in *Dnah11* [Hummel and Chapman 1959]) background and analyzed YGRI of chr7, chr12, and chr18 in cortical *Emx1*$^+$ projection neurons (Figure 6A). However, contrary to the *in vitro* data (Armakolas and Klar 2007), we could not observe randomization (i.e., a drop of YGRI value to 1) of sister chromatid segregation for the three tested chromosomes (chr7, chr12, and chr18). These data suggest that cultured differentiated ESC lineages and cortical excitatory neurons *in vivo* differ in mechanisms of biased sister chromatid segregation.

Chromosome-specific biases of sister chromatid segregation differ in distinct cell types

To determine the possible influence of cell type on biased, chromosome-specific, sister chromatid segregation patterns, we first analyzed *Emx1*$^+$ cortical astrocytes and hippocampal CA1 pyramidal cells. The YGRI for cortical astrocytes was markedly different from the YGRI for cortical projection neurons or hippocampal CA1 pyramidal cells for a representative set of 10 MADM chromosomes analyzed (Figures 6B and 6C). Next, we introduced *Nestin*-Cre to label neural lineages beyond forebrain projection neurons and astrocytes. We focused on cerebellar Purkinje cells and determined the YGRI. Strikingly, the YGRI for Purkinje cells was also markedly different in most MADMs compared to the YGRIs for cortical projection neurons and astrocytes and hippocampal CA1 pyramidal cells (Figures 6B and 6C).

Finally, we assessed sister chromatid segregation patterns for a non-neural somatic cell type. We focused on T cells (CD3$^+$) and B cells (CD19$^+$) within the hematopoietic lineage and determined the YGRI for six different MADM chromosomes by fluorescence-activated cell sorting (FACS) analysis (Figure 6D). Although the distinct MADM chromosomes showed different YGRI values, the YGRI for T cells in comparison to B cells was not significantly different for all six chromosomes analyzed. No significant

Figure 4. MADM-induced uniparental chromosome disomy (UPD) results in paternal growth dominance in liver

(A) MADM scheme for imprinted genes. G2-X MADM events generate differentially labeled cells with near-complete UPD (cells with two copies of either the maternal [matUPD] or the paternal [patUPD] chromosome). (Top) The GT MADM cassette is inherited from the mother (M, pink) and the TG MADM cassette from the father (P, blue), and green cells show patUPD (PP) and red cells matUPD (MM). In such a scenario, imprinted maternally expressed genes are expressed at twice the normal dose and paternally expressed genes are not expressed in cells with matUPD (red). In contrast, paternally expressed genes are overexpressed by factor two and maternally expressed genes are not expressed in cells with patUPD (green). (Bottom) Reverse scheme with GT MADM cassette inherited from father and TG MADM cassette inherited from mother. Here, cells with matUPD are labeled in green and cells with patUPD in red fluorescent color.

(B–U) Representative images of horizontal liver cryosections with MADM labeling (GFP, green; tdT, red) in MADM-1 (A) to MADM-19 (T and U) in combination with *Hprt*-Cre driver at P21. Higher resolution image (U) represents inset in (T) in left lateral lobe of liver in MADM-19.

(V) (Top) Representative images (left, middle) of liver in *MADM-7*$^{GT/TG}$;*Hprt*$^{Cre/+}$ with green GFP$^+$ patUPD and red tdT$^+$ matUPD (*left*) or red tdT$^+$ patUPD and green GFP$^+$ matUPD (middle) at P21; and quantification (right) of absolute (cells/mm^3) and relative (PP/MM) numbers of MADM-labeled cells with UPD. (Middle) Representative images (left, middle) of liver in *MADM-11*$^{GT/TG}$;*Hprt*$^{Cre/+}$ with green GFP$^+$ patUPD and red tdT$^+$ matUPD (left) or red tdT$^+$ patUPD and green GFP$^+$ matUPD (middle) at P21; and quantification (right) of absolute (cells/mm^3) and relative (PP/MM) numbers of MADM-labeled cells with UPD. (Bottom) Representative images (left, middle) of liver in *MADM-17*$^{GT/TG}$;*Hprt*$^{Cre/+}$ with green GFP$^+$ patUPD and red tdT$^+$ matUPD (left) or red tdT$^+$ patUPD and green GFP$^+$ matUPD (middle) at P21; and quantification (right) of absolute (cells/mm^2) and relative (PP/MM) numbers of MADM-labeled cells with UPD. Nuclei were stained using DAPI. Bars represent mean ± SEM. Data show *MADM-7*$^{GT/TG}$;*Hprt*$^{Cre/+}$ n = 6, *MADM-11*$^{GT/TG}$;*Hprt*$^{Cre/+}$ n = 5, *MADM-17*$^{GT/TG}$;*Hprt*$^{Cre/+}$ n = 6 mice. Scale bar: 200 μm.

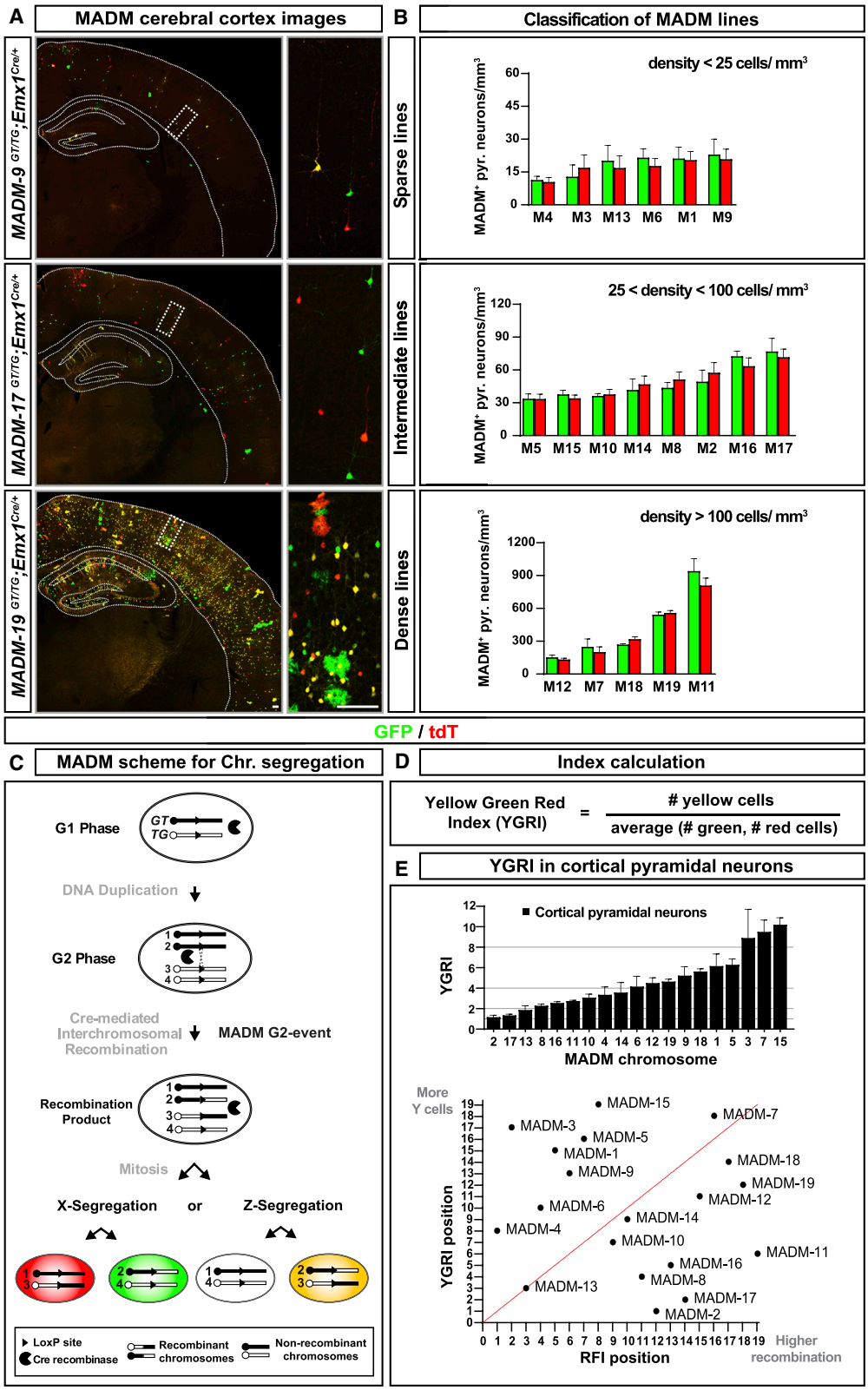

(legend on next page)

correlation could be established when the YGRI of T/B cells was compared to the YGRI of the neural lineages. Altogether, these data indicate that the highly biased and chromosome-specific sister chromatid segregation patterns are further affected by cell type in somatic cell lineages *in vivo*.

DISCUSSION

The analysis of gene function in multicellular systems *in vivo* requires quantitative and high-resolution experimental tools to analyze the cellular phenotype. Here, we expanded the MADM technology to enable, in principle, the genetic mosaic dissection of cell-autonomous gene function of most genes (>96%) across the entire mouse genome with single-cell resolution. Although functional genetic mosaic analysis clearly represents the most salient utility of MADM, we also extended the application spectrum and used MADM as a proxy to trace the randomness of mitotic sister chromatid segregation patterns upon somatic stem cell division. We first discuss these biological findings in a more general context before we elaborate on the overarching potential of the genome-wide MADM resource for future genetic mosaic analysis.

Non-random mitotic sister chromatid segregation in mouse *in vivo*

Asymmetric stem cell division requires the non-equivalent distribution of cell-fate determinants including proteins, mRNA, or intracellular organelles (Gönczy 2008; Knoblich 2008; Taverna et al., 2014). Recently, an intriguing model has been postulated whereby asymmetric cell division might also be promoted by differentiation of sister chromatids by epigenetic means, followed by selective segregation of "unequal" sister chromatids to daughter cells (Bell 2005; Armakolas et al., 2010; Yamashita 2013). However, experimental evidence supporting such a model in mice was so far obtained solely from *in vitro* studies in ESCs and derived lineages and only for one chromosome (chr7; Figure 7, left; Liu et al., 2002; Armakolas and Klar 2006). In our study we systematically traced sister chromatid segregation patterns of the entire set of mouse autosomes *in vivo*. We observed that the prevalence of G2-X events, approximated in the value of YGRI, in the same cell type (cortical projection neurons) and by using identical an *Emx1*-Cre driver vastly differed, up to one order of magnitude for different chromosomes. However, the relative amount of G2-X segregation did not correlate with the absolute recombination frequency. Thus, high absolute recombination frequency does not predict a bias in recombinant sister chromatid segregation toward G2-X nor G2-Z. Previous work has postulated that it is highly unlikely that biased sister chromatid segregation may have evolved for a site-specific recombination system not indigenous to mouse cells (Armakolas et al., 2010). Yet, we note that the dynamic state of chromatin architecture may influence absolute recombination frequency (proximity of *loxP* sites). We also cannot exclude that the location of the genomic recombination loci, and thus the size of resulting recombinant sister chromatids, may influence segregation bias. Such a hypothesis may be tested in the future by systematic introduction of *loxP* sites at defined genomic distance intervals.

Our observation that distinct cell types show different YGRI for the same chromosome could reflect a different recombination activity of respective Cre drivers in a particular cellular lineage. For our MADM-based analysis, we used *Emx1*- and *Nestin*-Cre drivers that are mostly active in dividing neural stem cells and turned off in postmitotic cells. The contribution of G_0 recombination is thus expected to be minimal. Still, all YGRIs in neural lineages were ≥ 1, with some up to an order of magnitude higher indicating increasing rates of G2-Z segregation. However, a certain rate of G1 recombination (also producing yellow cells that increase the YGRI) besides G2-Z segregation may add to the overall YGRI. Although G1 recombination events did not occur in cultured ESCs (Liu et al., 2002; Armakolas and Klar 2006), we cannot currently exclude that interchromosomal recombination efficiency could be distinct in G1 versus G2 phases of the cell cycle for different cell types *in vivo*. However, for any given cell division cycle, the relative recombination events in G1 versus G2 should be the same. Thus, different YGRIs for different chromosomes must reflect chromosome-specific sister chromatid segregation patterns in genetically identical cells (here, *Emx1*$^+$ cortical projection neurons). Perhaps most striking was the finding that YGRIs of 10 different chromosomes in astrocytes were rather constant and low, indicating a

Figure 5. Mitotic interchromosomal recombination efficiency and sister chromatid segregation patterns for all MADM reporters in cortical projection neurons

(A) Representative images of MADM-labeling pattern (green, GFP; red, tdT; yellow, GFP/tdT) in cerebral cortex in three exemplary MADM lines in combination with the *Emx1*-Cre driver at P21. (Top) *MADM-9*$^{GT/TG}$;*Emx1*$^{Cre/+}$; (middle) *MADM-17*$^{GT/TG}$;*Emx1*$^{Cre/+}$; (bottom) *MADM-19*$^{GT/TG}$;*Emx1*$^{Cre/+}$. Scale bar: 100 μm.

(B) Classification of MADM lines. (Top) Sparse (< 25 cells/mm^3). (Middle) Intermediate (25–100 cells/mm^3). (Bottom) Dense (>100 cells/mm^3). Bars represent mean ± SEM. Data show M7, M11, and M19 (n = 5); M2, M3, M5, M8–M10, and M12–M18 (n = 6); M4 and M6 (n = 8), and M1 (n = 12 mice).

(C) MADM principle illustrating G2-X and G2-Z segregation patterns. Upon Cre-mediated interchromosomal recombination at the *loxP* site in the MADM cassettes in G2 phase of the cell cycle, recombinant chromosomes can either segregate together to the same daughter cell (G2-Z segregation; yellow, GFP/tdT and unlabeled cell) or each recombinant chromosome may segregate to distinct daughter cells (G2-X segregation; green, GFP$^+$ and red tdT$^+$ cell, respectively) upon mitosis.

(D) Definition of yellow-green-red-index index (YGRI). The YGRI is calculated from the number of yellow cells divided by the average of green and red cells to compensate for G2-Z events that leads to labeling of only one daughter cell (yellow) and an (invisible) unlabeled cell. Note that yellow cells emerging from G1/G_0 events contribute to the total number of yellow cells.

(E) YGR index in neuronal lineages. (Top) YGRI for cortical projection neurons in P21 neocortex of all 19 MADM reporter lines in combination with the *Emx1*-Cre driver. Note that (1) YGRI varies from 1 to 10 but is never below 1 and (2) YGRIs do not correlate with the sizes of the respective MADM chromosomes. Bars represent mean ± SEM. Data show M2, M3, M5, and M7–M19 (n = 6); M4 and M6 (n = 8); and M1 (n = 12). (Bottom) YGRI ranking in correlation (red line) to recombination frequency index (RFI). Note that MADM chromosomes with a high recombination frequency do not necessarily present high YGRI and vice versa. See also Figures S1 and S9.

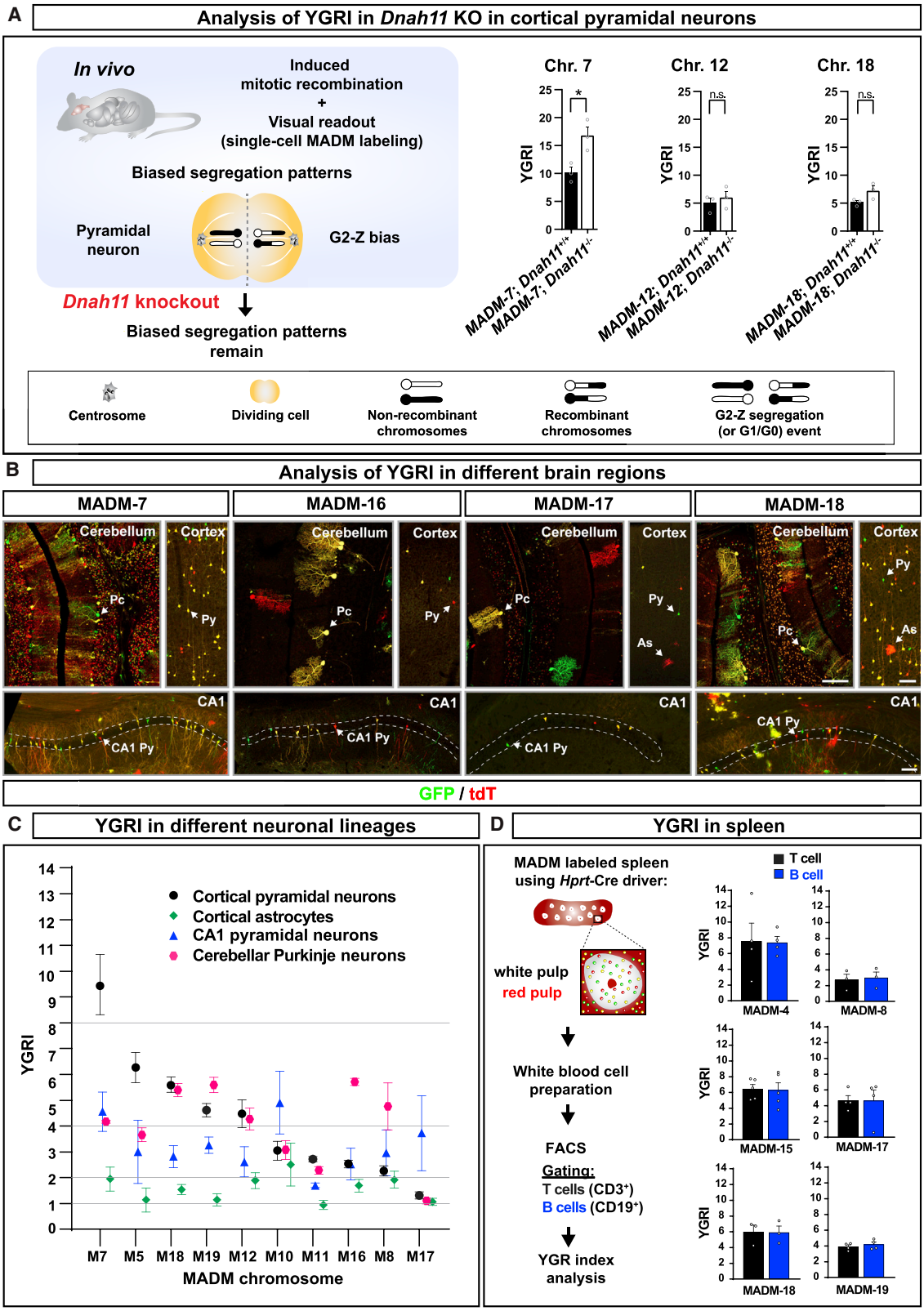

(legend on next page)

uniformly high relative frequency for G2-X events in astrocyte progenitors, which is in stark contrast to the values for the same chromosomes in projection neurons that emerge also from the same (*Emx1*$^+$) stem cell lineage. Thus, sister chromatid segregation appears highly biased in a chromosome-specific manner in mitotic cortical *Emx1*$^+$ progenitors. Furthermore, the rank orders of YGRI for each chromosome in different cell types were not the same, suggesting that the bias of sister chromatid segregation patterns results from a complex combination of chromosome and cell-type-specific mechanisms (Figure 7, right).

Previous studies found that cultured ESC clones that were differentiated into an neuroectoderm lineage never showed G2-X segregation (Liu et al., 2002; Armakolas and Klar 2006). These findings are in stark contrast to our *in vivo* results that demonstrate for all 19 mouse autosomes a substantial amount of G2-X segregation in at least 4 distinct neural cell lineages. Furthermore, our analysis of *Dnah11* indicates that the involved molecular mechanisms likely differ (at least for chr7) when comparing cell culture to intact brain tissue. We cannot fully explain the cause of the differences in results obtained in cell culture and *in vivo*, but systemic and/or tissue-wide acting mechanisms could be involved (Knouse et al., 2018).

The phenomenon of biased sister chromatid segregation appears to be evolutionarily conserved (Pimpinelli and Ripoll 1986; Beumer et al., 1998). In asymmetrically dividing male germline stem cells in *Drosophila*, sister chromatids of X and Y, but not autosomes, are segregated non-randomly (Yadlapalli and Yamashita 2013). In such a context, SUN-KASH proteins, proposed to anchor sister chromatids to the centrosome, seem to be involved, besides regulators of DNA methylation (Yadlapalli and Yamashita 2013). Although the underlying molecular mechanisms may or may not be conserved, it will be intriguing to assess the physiological function in future studies and experimentally approach the hypothesis postulating that biased sister chromatid segregation could be a mechanism to instruct the cell fate of nascent daughter cells during asymmetric stem cell division (Bell 2005; Armakolas et al., 2010; Yadlapalli and Yamashita 2013). Because MADM enables both clonal lineage tracing with concurrent genetic manipulation, such an approach promises high potential to systematically address the physiological role of biased sister chromatid segregation in the future.

Genome-wide MADM mice library for single-cell genetic mosaic analysis

Genetic dissection of cell-autonomous gene function and system-wide effects

The MADM technology enables a variety of genetic *in vivo* paradigms to study a broad spectrum of cell and developmental processes (Zong et al., 2005; Luo 2007; Muzumdar et al., 2007; Hippenmeyer 2013; Hippenmeyer et al., 2013). One exclusive application of the MADM system is the feature enabling the genetic dissection of the relative contributions of cell-autonomous and extrinsic systemic and/or tissue-wide components to the overall cellular phenotype upon the loss of candidate gene function (Hansen and Hippenmeyer 2020). In fact, single-cell phenotypes in classical conditional or full knockout mutants often reflect a combination of both cell-autonomous gene function and environment-derived cues that may remedy or exacerbate any observed phenotype. It is thus important to qualitatively and quantitatively determine the relative contribution of the intrinsic and extrinsic components to the overall loss of the gene function phenotype. To this end, the MADM system offers an unmatched experimental solution. The candidate gene function can be either ablated in a very sparse mosaic (or single clones) or tissue wide in all cells. Yet, in both paradigms, single-cell MADM labeling enables the high-resolution quantitative phenotypic analysis (Joo et al., 2014; Beattie et al., 2017; Laukoter et al., 2020b; Takeo et al., 2021). The MADM lines in conjunction with the above paradigms thus potentially permit the systematic dissection of the level of cell autonomy of any gene function in a given tissue, provided appropriate Cre driver lines exist. Insights at the single-cell resolution as obtained from MADM-based approaches in combination with systematic candidate gene interrogation (Beattie et al., 2017; Laukoter et al., 2020b) likely will have implications for our general understanding of diseases including neurodevelopmental disorders (D'Gama and Walsh 2018; Jayaraman et al., 2018; Buchsbaum and Cappello 2019; Pinson et al., 2019; Subramanian et al., 2020).

Figure 6. Sister chromatid segregation patterns based on YGRI in *Dnah11* knockout (KO) and in different somatic cell lineages

(A) (Left) Summary of YGRI analysis in selected MADM reporters with *Dnah11* depletion (in *iv* mice). (Right) YGR index for cortical projection neurons in P21 neocortex in MADM-7, MADM-12, and MADM-18 reporter lines in combination with the *Emx1*-Cre driver in control and *Dnah11* KO (*iv*) mice. Note that a decrease of YGRI to 1 would indicate random sister chromatid segregation but that the YGRI was not decreased upon *Dnah11* mutation. Bars represent mean ± SEM. Data show n = 3 mice for each genotype.

(B) Representative confocal microscopy images at P21 with MADM labeling (GFP, green; tdT, red) from selected MADM reporters in combination with a *Nestin*-Cre (cerebellum) or *Emx1*-Cre (cerebral cortex and hippocampal CA1 area) driver used for quantifications in Figures 5C and 6A. Arrows indicate Purkinje cells (Pcs), cortical pyramidal neurons (Pys), and CA1 pyramidal neurons (CA1 Pys). Scale bar: 100 μm.

(C) YGRI for selected MADM reporters in different neuronal lineages at P21. YGRI of cortical astrocytes and hippocampal CA1 pyramidal cells derived from *Emx1*$^+$ progenitors and cerebellar Purkinje cells derived from *Nestin*$^+$ progenitors significantly differ from the YGRI of cortical pyramidal neurons for most MADM chromosomes analyzed. Values represent mean ± SEM. Data show pyramidal neurons (n = 6); cortical astrocytes (n = 6); CA1 pyramidal neurons M5, M7, M8, M11, M12, M16, M18, and M19 (n = 6); M10 (n = 7); M17 (n = 8); cerebellar Purkinje cells M7, M8, M11, M16, M17, and M19 (n = 3); M12 and M18 (n = 4); M10 (n = 5) and M5 (n = 6 mice).

(D) (Left) White blood cell preparations from spleen in MADM reporters with *Hprt*-Cre at P21 were subjected to FACS. The number of green GFP$^+$, red tdT$^+$, and yellow GFP$^+$/tdT$^+$ CD3$^+$ T cells (black) and CD19$^+$ B cells (blue) were quantified. (Right) YGRI for six different MADM chromosomes including sparse (MADM-4), intermediate (MADM-8, MADM-15, and MADM-17), and dense (MADM-18 and MADM-19) lines. The different MADM recombinant chromosomes displayed distinct YGRI but YGRI for T cells and B cells was not significantly different for all MADM chromosomes analyzed. Bars represent mean ± SEM. Data show M8 and M18 (n = 3); M4, M17, and M19 (n = 4); M15 (n = 5 mice). Welch's unequal variances t test, p_{M4} = 7.5E−01, p_{M8} = 7.9E−01, p_{M15} = 7.7E−01, p_{M17} = 6.4E−01, p_{M18} = 9.8E−01, p_{M19} = 5.0E−01.

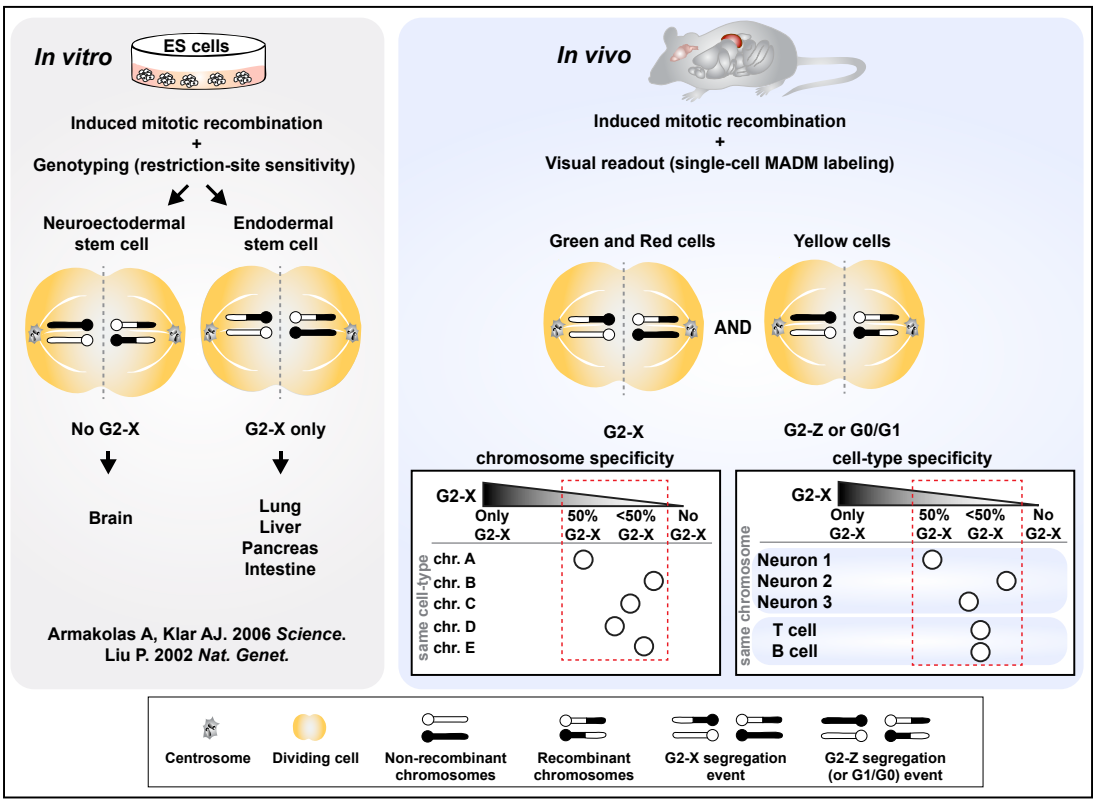

Figure 7. Models of biased sister chromatid segregation patterns in ESCs *in vitro* and in mouse *in vivo*

(Left) Previous studies (Liu et al., 2002; Armakolas and Klar 2006) using mitotic recombination and in combination with restriction-site sensitivity for genotyping in ESC cultures reported that in ESC-derived neuroectodermal lineages no G2-X (recombinant chromosomes segregate away from each other during cell division) events could be observed. In contrast, lineages derived from endodermal stem cells showed exclusively G2-X segregation patterns. Based on these findings, it could be anticipated that in MADM there would be no red and green cells in neural lineages (e.g., in the brain), which was not the case for all MADM chromosomes. (Right) *In vivo* analysis of the prevalence of G2-X events (red and green cells) in comparison with total number of yellow cells (G2-Z, G1, and G_0 events) for all MADM chromosomes and in several somatic cell lineages revealed a significant bias in the recombinant chromosome and thus sister chromatid segregation patterns. The segregation bias showed marked chromosome specificity that was distinct for different chromosomes in the same cell type in both brain and hematopoietic systems. The segregation bias appears also to be affected by cell type, as the level of bias was distinct for the same chromosome in different cell types.

Single-cell analysis of imprinting phenotypes in UPD

One MADM application includes the property to generate cells with UPD and thus enable the study of imprinting phenotypes at a single-cell level (Hippenmeyer et al., 2013; Laukoter et al., 2020a, 2020c). In fact, technical limitations so far only allowed the investigation of UPD at the whole-animal level but lacked the resolution to obtain insights at the cellular level (Pauler et al., 2021). It will be revealing in future studies to systematically probe the cell-autonomous consequences of UPD at a single-cell level and without inducing global changes in imprinted gene expression affecting the whole animal. The library of all 19 MADM reporters will in principle enable the systematic analysis of UPD-associated cellular phenotypes in any organ, tissue, and cell type in the mouse. Importantly, the analysis of candidate gene function, i.e., loss-of-function phenotypes, can be separated from UPD-mediated imprinting phenotypes by reverse MADM breeding schemes (Hippenmeyer et al., 2010, 2013; Joo et al., 2014; Beattie et al., 2017; Laukoter et al., 2020b).

One possible limitation or confounder for the interpretation of MADM-based cell labeling and gene dosage is cellular polyploidy (Øvrebø and Edgar 2018). It will thus be crucial in the future to carefully analyze in organs with polyploid cells (1) whether more than one individual recombination event can occur and (2) at which frequency. Depending on the probability of multiple recombination events, the color/tone of the overall MADM labeling, and thus gene dosage, could be distinct from the above predicted scenario for UPD and potentially offer an assay for studying gene dosage across multiple scales. In a broader context, because UPD in humans is associated with a variety of diseases (Feinberg 2007; Tuna et al., 2009; Yamazawa et al., 2010; Buiting et al., 2016) MADM-based analysis will also contribute to our general understanding of the underlying etiology of imprinting disorders at the single-cell level.

Analysis of cellular competition at single-cell level in health and disease

MADM can be exploited for the study of cellular competition in a developmental context (Joo et al., 2014; Takeo et al., 2021). For

instance, when the TrkC neurotrophin receptor is removed sparsely with MADM from just a few individual Purkinje cells in the cerebellum, their dendrites have fewer and shorter branches. In contrast, when TrkC is ablated from all Purkinje cells, the dendrite trees look normal. Thus, a competitive mechanism could be involved whereby the shape of the dendrite tree depends on relative differences in neurotrophin/TrkC signaling between Purkinje cell neighbors (Joo et al., 2014). Purkinje cell dendritic arbors have also been shown to depend on GluD2- and Cbln1-mediated competitive interactions (Takeo et al., 2021). Cell competition has not only been implicated in cell morphogenesis but also extensively studied in a variety of contexts. Cell competition is particularly critical for overall tissue homeostasis during growth and regeneration but also for cell mixing and tissue invasion in cancer (Merino et al., 2016; Brás-Pereira and Moreno 2018; Madan et al., 2018; Ellis et al., 2019). With the availability of MADM for all mouse autosomes, the phenomenon of cell competition can be studied holistically and for virtually any candidate gene function associated with it in diverse biological contexts in health and disease.

Although MADM technology is versatile and offers multiple applications (discussed above), the method also has certain limitations and alternative systems may be considered depending on the biological question and context (Garcia-Gonzalez et al., 2020; Hansen and Hippenmeyer 2020). For instance, the expression of the two markers relies on a single-copy insertion and thus the expression level may be lower than, for example, that in viral-based systems. Optimization of the MADM reporter expression by using amplification systems such as, for example, the TIGRE (Madisen et al., 2015; Daigle et al., 2018) might offer a solution. Unlike TIGRE-based systems, MADM currently cannot be used to monitor physiological processes, but creating split transgenes of diverse reporters in future could enable such applications in clonally related cells in wild-type and potentially in a mutant context. Although MADM can be used in combination with temporal TM/CreER induction to label individual clones emerging from dividing stem cells, the system cannot be used to sparsely label and genetically manipulate postmitotic cells. Also, MADM currently cannot be easily used for the overexpression of transgenes in a mosaic setting. However, a number of recently developed systems—such as MASTR (Lao et al., 2012), Dual ifgMosaic (Pontes-Quero et al., 2017), iSuRe-Cre (Fernández-Chacón et al., 2019), MADR (Kim et al., 2019), or BATTLE (Kohara et al., 2020) among others—allow for sparse and tunable mosaic labeling and/or genetic manipulation including overexpression of transgenes in postmitotic cells in a variety of cellular contexts. However, a clear advantage over the above methods and special property of MADM relies on the built-in control with two distinct fluorescent colors for mutant analysis and the functional assessment of gene dosage. Thus, MADM can be used for unparalleled comparative mutant versus heterozygote and control analysis at once and at a single-cell resolution in any given tissue *in situ*.

Lastly, MADM technology based on gene targeting in ESCs is currently available only in mice. Future expansion of the system to other species by endonuclease-mediated transgenesis like CRISPR-Cas9 technology can be anticipated. Altogether, the genome-wide MADM resource presented in this study likely will catalyze the genetic dissection of cell-autonomous gene function and thus molecular mechanisms with single-cell resolution across a broad spectrum of biological questions in health and disease.

STAR★METHODS

Detailed methods are provided in the online version of this paper and include the following:

- KEY RESOURCES TABLE
- RESOURCE AVAILABILITY
  - Lead contact
  - Materials availability
  - Data and code availability
- EXPERIMENTAL MODEL AND SUBJECT DETAILS
  - Generation, breeding and husbandry of mouse lines
- METHOD DETAILS
  - Molecular biology
  - Generation of transgenic MADM mice
  - Genotyping of MADM reporters, *Apc*-flox and *iv* mice
  - Isolation of MADM-labeled tissue
  - Histology and immunostaining of MADM-labeled tissue
  - Flow cytometry
  - Analysis of MADM-labeled brains and peripheral tissue
- QUANTIFICATION AND STATISTICAL ANALYSIS

SUPPLEMENTAL INFORMATION

Supplemental information can be found online at https://doi.org/10.1016/j.celrep.2021.109274.

ACKNOWLEDGMENTS

We thank the Bioimaging, Life Science, and Pre-Clinical Facilities at IST Austria; M.P. Postiglione, C. Simbriger, K. Valoskova, C. Schwayer, T. Hussain, M. Pieber, and V. Wimmer for initial experiments, technical support, and/or assistance; R. Shigemoto for sharing *iv* (*Dnah11* mutant) mice; and M. Sixt and all members of the Hippenmeyer lab for discussion. This work was supported by National Institutes of Health grants (R01-NS050580 to L.L. and F32MH096361 to L.A.S.). L.L. is an investigator of HHMI. N.A. received support from FWF Firnberg-Programm (T 1031). A.H.H. is a recipient of a DOC Fellowship (24812) of the Austrian Academy of Sciences. This work also received support from IST Austria institutional funds, FWF SFB F78 to S.H., the People Programme (Marie Curie Actions) of the European Union's Seventh Framework Programme (FP7/2007-2013) under REA grant agreement no 618444 to S.H., and the European Research Council (ERC) under the European Union's Horizon 2020 Research and Innovation Programme (grant agreement no. 725780 LinPro) to S.H.

AUTHOR CONTRIBUTIONS

S.H. and L.L. conceived the research. S.H., L.L., L.A.S., T.R., N.A,. and X.C. designed all experiments and interpreted the data. X.C., A.D., N.A., A.H.H., J.S., L.A., T.B., T.R., L.A.S., A.H., C.S., and R.L.J. performed all the experiments. S.H. wrote the manuscript with inputs from L.L., N.A., and X.C. All authors edited and proofread the manuscript.

DECLARATION OF INTERESTS

The authors declare no competing interests.

Received: September 9, 2020
Revised: April 14, 2021
Accepted: May 28, 2021
Published: June 22, 2021

REFERENCES

Ali, S.R., Hippenmeyer, S., Saadat, L.V., Luo, L., Weissman, I.L., and Ardehali, R. (2014). Existing cardiomyocytes generate cardiomyocytes at a low rate after birth in mice. Proc. Natl. Acad. Sci. USA *111*, 8850–8855.

Amberg, N., Holcmann, M., Glitzner, E., Novoszel, P., Stulnig, G., and Sibilia, M. (2015). Mouse models of nonmelanoma skin cancer. Methods Mol. Biol. *1267*, 217–250.

Apte, M.S., and Meller, V.H. (2012). Homologue pairing in flies and mammals: gene regulation when two are involved. Genet. Res. Int. *2012*, 430587.

Armakolas, A., and Klar, A.J. (2006). Cell type regulates selective segregation of mouse chromosome 7 DNA strands in mitosis. Science *311*, 1146–1149.

Armakolas, A., and Klar, A.J. (2007). Left-right dynein motor implicated in selective chromatid segregation in mouse cells. Science *315*, 100–101.

Armakolas, A., Koutsilieris, M., and Klar, A.J. (2010). Discovery of the mitotic selective chromatid segregation phenomenon and its implications for vertebrate development. Curr. Opin. Cell Biol. *22*, 81–87.

Barker, N., van Es, J.H., Kuipers, J., Kujala, P., van den Born, M., Cozijnsen, M., Haegebarth, A., Korving, J., Begthel, H., Peters, P.J., and Clevers, H. (2007). Identification of stem cells in small intestine and colon by marker gene Lgr5. Nature *449*, 1003–1007.

Barker, N., Ridgway, R.A., van Es, J.H., van de Wetering, M., Begthel, H., van den Born, M., Danenberg, E., Clarke, A.R., Sansom, O.J., and Clevers, H. (2009). Crypt stem cells as the cells-of-origin of intestinal cancer. Nature *457*, 608–611.

Beattie, R., Postiglione, M.P., Burnett, L.E., Laukoter, S., Streicher, C., Pauler, F.M., Xiao, G., Klezovitch, O., Vasioukhin, V., Ghashghaei, T.H., and Hippenmeyer, S. (2017). Mosaic Analysis with Double Markers Reveals Distinct Sequential Functions of Lgl1 in Neural Stem Cells. Neuron *94*, 517–533.e3.

Beattie, R., Streicher, C., Amberg, N., Cheung, G., Contreras, X., Hansen, A.H., and Hippenmeyer, S. (2020). Lineage Tracing and Clonal Analysis in Developing Cerebral Cortex Using Mosaic Analysis with Double Markers (MADM). J. Vis. Exp. (*159*) https://doi.org/10.3791/61147.

Behrens, J., Jerchow, B.A., Würtele, M., Grimm, J., Asbrand, C., Wirtz, R., Kühl, M., Wedlich, D., and Birchmeier, W. (1998). Functional interaction of an axin homolog, conductin, with beta-catenin, APC, and GSK3beta. Science *280*, 596–599.

Bell, C.D. (2005). Is mitotic chromatid segregation random? Histol. Histopathol. *20*, 1313–1320.

Beumer, K.J., Pimpinelli, S., and Golic, K.G. (1998). Induced chromosomal exchange directs the segregation of recombinant chromatids in mitosis of Drosophila. Genetics *150*, 173–188.

Biesecker, L.G., and Spinner, N.B. (2013). A genomic view of mosaicism and human disease. Nat. Rev. Genet. *14*, 307–320.

Brás-Pereira, C., and Moreno, E. (2018). Mechanical cell competition. Curr. Opin. Cell Biol. *51*, 15–21.

Buchsbaum, I.Y., and Cappello, S. (2019). Neuronal migration in the CNS during development and disease: insights from *in vivo* and *in vitro* models. Development *146*, dev163766.

Buiting, K., Williams, C., and Horsthemke, B. (2016). Angelman syndrome—insights into a rare neurogenetic disorder. Nat. Rev. Neurol. *12*, 584–593.

Cheung, A.F., Carter, A.M., Kostova, K.K., Woodruff, J.F., Crowley, D., Bronson, R.T., Haigis, K.M., and Jacks, T. (2010). Complete deletion of Apc results in severe polyposis in mice. Oncogene *29*, 1857–1864.

D'Gama, A.M., and Walsh, C.A. (2018). Somatic mosaicism and neurodevelopmental disease. Nat. Neurosci. *21*, 1504–1514.

Daigle, T.L., Madisen, L., Hage, T.A., Valley, M.T., Knoblich, U., Larsen, R.S., Takeno, M.M., Huang, L., Gu, H., Larsen, R., et al. (2018). A Suite of Transgenic Driver and Reporter Mouse Lines with Enhanced Brain-Cell-Type Targeting and Functionality. Cell *174*, 465–480.e22.

Ellis, S.J., Gomez, N.C., Levorse, J., Mertz, A.F., Ge, Y., and Fuchs, E. (2019). Distinct modes of cell competition shape mammalian tissue morphogenesis. Nature *569*, 497–502.

Espinosa, J.S., Wheeler, D.G., Tsien, R.W., and Luo, L. (2009). Uncoupling dendrite growth and patterning: single-cell knockout analysis of NMDA receptor 2B. Neuron *62*, 205–217.

Feinberg, A.P. (2007). Phenotypic plasticity and the epigenetics of human disease. Nature *447*, 433–440.

Fernández-Chacón, M., Casquero-García, V., Luo, W., Francesca Lunella, F., Ferreira Rocha, S., Del Olmo-Cabrera, S., and Benedito, R. (2019). iSuRe-Cre is a genetic tool to reliably induce and report Cre-dependent genetic modifications. Nat. Commun. *10*, 2262.

Ferreira, R.M.M., Sancho, R., Messal, H.A., Nye, E., Spencer-Dene, B., Stone, R.K., Stamp, G., Rosewell, I., Quaglia, A., and Behrens, A. (2017). Duct- and Acinar-Derived Pancreatic Ductal Adenocarcinomas Show Distinct Tumor Progression and Marker Expression. Cell Rep. *21*, 966–978.

Fodde, R., Smits, R., and Clevers, H. (2001). APC, signal transduction and genetic instability in colorectal cancer. Nat. Rev. Cancer *1*, 55–67.

Fuchs, E., and Nowak, J.A. (2008). Building epithelial tissues from skin stem cells. Cold Spring Harb. Symp. Quant. Biol. *73*, 333–350.

Gao, P., Postiglione, M.P., Krieger, T.G., Hernandez, L., Wang, C., Han, Z., Streicher, C., Papusheva, E., Insolera, R., Chugh, K., et al. (2014). Deterministic progenitor behavior and unitary production of neurons in the neocortex. Cell *159*, 775–788.

Garcia-Gonzalez, I., Mühleder, S., Fernández-Chacón, M., and Benedito, R. (2020). Genetic Tools to Study Cardiovascular Biology. Front. Physiol. *11*, 1084.

Germani, F., Bergantinos, C., and Johnston, L.A. (2018). Mosaic Analysis in *Drosophila*. Genetics *208*, 473–490.

Gönczy, P. (2008). Mechanisms of asymmetric cell division: flies and worms pave the way. Nat. Rev. Mol. Cell Biol. *9*, 355–366.

Gonzalez, P.P., Kim, J., Galvao, R.P., Cruickshanks, N., Abounader, R., and Zong, H. (2018). p53 and NF 1 loss plays distinct but complementary roles in glioma initiation and progression. Glia *66*, 999–1015.

Gorski, J.A., Balogh, S.A., Wehner, J.M., and Jones, K.R. (2003). Learning deficits in forebrain-restricted brain-derived neurotrophic factor mutant mice. Neuroscience *121*, 341–354.

Haig, D. (2004). Genomic imprinting and kinship: how good is the evidence? Annu. Rev. Genet. *38*, 553–585.

Hansen, A.H., and Hippenmeyer, S. (2020). Non-Cell-Autonomous Mechanisms in Radial Projection Neuron Migration in the Developing Cerebral Cortex. Front. Cell Dev. Biol. *8*, 574382.

Henderson, N.T., Le Marchand, S.J., Hruska, M., Hippenmeyer, S., Luo, L., and Dalva, M.B. (2019). Ephrin-B3 controls excitatory synapse density through cell-cell competition for EphBs. eLife *8*, e41563.

Hippenmeyer, S. (2013). Dissection of gene function at clonal level using mosaic analysis with double markers. Front. Biol. *8*, 557–568.

Hippenmeyer, S., Youn, Y.H., Moon, H.M., Miyamichi, K., Zong, H., Wynshaw-Boris, A., and Luo, L. (2010). Genetic mosaic dissection of Lis1 and Ndel1 in neuronal migration. Neuron *68*, 695–709.

Hippenmeyer, S., Johnson, R.L., and Luo, L. (2013). Mosaic analysis with double markers reveals cell-type-specific paternal growth dominance. Cell Rep. *3*, 960–967.

Hotta, Y., and Benzer, S. (1970). Genetic dissection of the Drosophila nervous system by means of mosaics. Proc. Natl. Acad. Sci. USA *67*, 1156–1163.

Hsu, Y.C., Li, L., and Fuchs, E. (2014). Emerging interactions between skin stem cells and their niches. Nat. Med. *20*, 847–856.

Hummel, K.P., and Chapman, D.B. (1959). Visceral inversion and associated anomalies in the mouse. J. Hered. *50*, 9–13.

Jayaraman, D., Bae, B.I., and Walsh, C.A. (2018). The Genetics of Primary Microcephaly. Annu. Rev. Genomics Hum. Genet. *19*, 177–200.

Joo, W., Hippenmeyer, S., and Luo, L. (2014). Neurodevelopment. Dendrite morphogenesis depends on relative levels of NT-3/TrkC signaling. Science *346*, 626–629.

Kim, G.B., Rincon Fernandez Pacheco, D., Saxon, D., Yang, A., Sabet, S., Dutra-Clarke, M., Levy, R., Watkins, A., Park, H., Abbasi Akhtar, A., et al. (2019). Rapid Generation of Somatic Mouse Mosaics with Locus-Specific, Stably Integrated Transgenic Elements. Cell *179*, 251–267.e24.

Knoblich, J.A. (2008). Mechanisms of asymmetric stem cell division. Cell *132*, 583–597.

Knouse, K.A., Lopez, K.E., Bachofner, M., and Amon, A. (2018). Chromosome Segregation Fidelity in Epithelia Requires Tissue Architecture. Cell *175*, 200–211.e13.

Kohara, K., Inoue, A., Nakano, Y., Hirai, H., Kobayashi, T., Maruyama, M., Baba, R., and Kawashima, C. (2020). BATTLE: Genetically Engineered Strategies for Split-Tunable Allocation of Multiple Transgenes in the Nervous System. iScience *23*, 101248.

Lao, Z., Raju, G.P., Bai, C.B., and Joyner, A.L. (2012). MASTR: a technique for mosaic mutant analysis with spatial and temporal control of recombination using conditional floxed alleles in mice. Cell Rep. *2*, 386–396.

Laukoter, S., Amberg, N., Pauler, F.M., and Hippenmeyer, S. (2020a). Generation and isolation of single cells from mouse brain with mosaic analysis with double markers-induced uniparental chromosome disomy. STAR Protoc. *1*, 100215.

Laukoter, S., Beattie, R., Pauler, F.M., Amberg, N., Nakayama, K.I., and Hippenmeyer, S. (2020b). Imprinted Cdkn1c genomic locus cell-autonomously promotes cell survival in cerebral cortex development. Nat. Commun. *11*, 195.

Laukoter, S., Pauler, F.M., Beattie, R., Amberg, N., Hansen, A.H., Streicher, C., Penz, T., Bock, C., and Hippenmeyer, S. (2020c). Cell-Type Specificity of Genomic Imprinting in Cerebral Cortex. Neuron *107*, 1160–1179.e9.

Lee, T., and Luo, L. (1999). Mosaic analysis with a repressible cell marker for studies of gene function in neuronal morphogenesis. Neuron *22*, 451–461.

Lee, T., and Luo, L. (2001). Mosaic analysis with a repressible cell marker (MARCM) for Drosophila neural development. Trends Neurosci. *24*, 251–254.

Lee, A.Y.L., Dubois, C.L., Sarai, K., Zarei, S., Schaeffer, D.F., Sander, M., and Kopp, J.L. (2019). Cell of origin affects tumour development and phenotype in pancreatic ductal adenocarcinoma. Gut *68*, 487–498.

Liang, H., Xiao, G., Yin, H., Hippenmeyer, S., Horowitz, J.M., and Ghashghaei, H.T. (2013). Neural development is dependent on the function of specificity protein 2 in cell cycle progression. Development *140*, 552–561.

Liu, P., Jenkins, N.A., and Copeland, N.G. (2002). Efficient Cre-loxP-induced mitotic recombination in mouse embryonic stem cells. Nat. Genet. *30*, 66–72.

Liu, C., Sage, J.C., Miller, M.R., Verhaak, R.G., Hippenmeyer, S., Vogel, H., Foreman, O., Bronson, R.T., Nishiyama, A., Luo, L., and Zong, H. (2011). Mosaic analysis with double markers reveals tumor cell of origin in glioma. Cell *146*, 209–221.

Lozano, G., and Behringer, R.R. (2007). New mouse models of cancer: single-cell knockouts. Proc. Natl. Acad. Sci. USA *104*, 4245–4246.

Luo, L. (2007). Fly MARCM and mouse MADM: genetic methods of labeling and manipulating single neurons. Brain Res. Brain Res. Rev. *55*, 220–227.

Lv, X., Ren, S.Q., Zhang, X.J., Shen, Z., Ghosh, T., Xianyu, A., Gao, P., Li, Z., Lin, S., Yu, Y., et al. (2019). TBR2 coordinates neurogenesis expansion and precise microcircuit organization via Protocadherin 19 in the mammalian cortex. Nat. Commun. *10*, 3946.

Madan, E., Gogna, R., and Moreno, E. (2018). Cell competition in development: information from flies and vertebrates. Curr. Opin. Cell Biol. *55*, 150–157.

Madisen, L., Garner, A.R., Shimaoka, D., Chuong, A.S., Klapoetke, N.C., Li, L., van der Bourg, A., Niino, Y., Egolf, L., Monetti, C., et al. (2015). Transgenic mice for intersectional targeting of neural sensors and effectors with high specificity and performance. Neuron *85*, 942–958.

Mähler Convenor, M., Berard, M., Feinstein, R., Gallagher, A., Illgen-Wilcke, B., Pritchett-Corning, K., and Raspa, M.; FELASA working group on revision of guidelines for health monitoring of rodents and rabbits (2014). FELASA recommendations for the health monitoring of mouse, rat, hamster, guinea pig and rabbit colonies in breeding and experimental units. Lab. Anim. *48*, 178–192.

Merino, M.M., Levayer, R., and Moreno, E. (2016). Survival of the Fittest: Essential Roles of Cell Competition in Development, Aging, and Cancer. Trends Cell Biol. *26*, 776–788.

Morgan, T.H., and Bridges, C.B. (1919). Contributions to the genetics of Drosophila melanogaster. The origin of gynandromorphs. Publs Carnegie Instn *278*, 1–122.

Muzumdar, M.D., Luo, L., and Zong, H. (2007). Modeling sporadic loss of heterozygosity in mice by using mosaic analysis with double markers (MADM). Proc. Natl. Acad. Sci. USA *104*, 4495–4500.

Muzumdar, M.D., Dorans, K.J., Chung, K.M., Robbins, R., Tammela, T., Gocheva, V., Li, C.M., and Jacks, T. (2016). Clonal dynamics following p53 loss of heterozygosity in Kras-driven cancers. Nat. Commun. *7*, 12685.

Ortiz-Álvarez, G., Daclin, M., Shihavuddin, A., Lansade, P., Fortoul, A., Faucourt, M., Clavreul, S., Lalioti, M.E., Taraviras, S., Hippenmeyer, S., et al. (2019). Adult Neural Stem Cells and Multiciliated Ependymal Cells Share a Common Lineage Regulated by the Geminin Family Members. Neuron *102*, 159–172.e7.

Øvrebø, J.I., and Edgar, B.A. (2018). Polyploidy in tissue homeostasis and regeneration. Development *145*, dev156034.

Pauler, F.M., Hudson, Q.J., Laukoter, S., and Hippenmeyer, S. (2021). Inducible uniparental chromosome disomy to probe genomic imprinting at single-cell level in brain and beyond. Neurochem. Int. *145*, 104986.

Petersen, P.H., Zou, K., Hwang, J.K., Jan, Y.N., and Zhong, W. (2002). Progenitor cell maintenance requires numb and numblike during mouse neurogenesis. Nature *419*, 929–934.

Pimpinelli, S., and Ripoll, P. (1986). Nonrandom segregation of centromeres following mitotic recombination in Drosophila melanogaster. Proc. Natl. Acad. Sci. USA *83*, 3900–3903.

Pinson, A., Namba, T., and Huttner, W.B. (2019). Malformations of Human Neocortex in Development - Their Progenitor Cell Basis and Experimental Model Systems. Front. Cell. Neurosci. *13*, 305.

Pontes-Quero, S., Heredia, L., Casquero-García, V., Fernández-Chacón, M., Luo, W., Hermoso, A., Bansal, M., Garcia-Gonzalez, I., Sanchez-Muñoz, M.S., Perea, J.R., et al. (2017). Dual ifgMosaic: A Versatile Method for Multispectral and Combinatorial Mosaic Gene-Function Analysis. Cell *170*, 800–814.e18.

Riccio, P., Cebrian, C., Zong, H., Hippenmeyer, S., and Costantini, F. (2016). Ret and Etv4 Promote Directed Movements of Progenitor Cells during Renal Branching Morphogenesis. PLoS Biol. *14*, e1002382.

Rossant, J., and Spence, A. (1998). Chimeras and mosaics in mouse mutant analysis. Trends Genet. *14*, 358–363.

Rülicke, T. (2004). Pronuclear microinjection of mouse zygotes. Methods Mol. Biol. *254*, 165–194.

Rülicke, T., Haenggli, A., Rappold, K., Moehrlen, U., and Stallmach, T. (2006). No transuterine migration of fertilised ova after unilateral embryo transfer in mice. Reprod. Fertil. Dev. *18*, 885–891.

Sambrook, J., Fritsch, E.F., and Maniatis, T. (1989). Molecular Cloning: a laboratory manual (Cold Spring Harbor Laboratory Press).

Schepers, A.G., Snippert, H.J., Stange, D.E., van den Born, M., van Es, J.H., van de Wetering, M., and Clevers, H. (2012). Lineage tracing reveals Lgr5+ stem cell activity in mouse intestinal adenomas. Science *337*, 730–735.

Smith, F.M., Garfield, A.S., and Ward, A. (2006). Regulation of growth and metabolism by imprinted genes. Cytogenet. Genome Res. *113*, 279–291.

Snippert, H.J., van der Flier, L.G., Sato, T., van Es, J.H., van den Born, M., Kroon-Veenboer, C., Barker, N., Klein, A.M., van Rheenen, J., Simons, B.D., and Clevers, H. (2010). Intestinal crypt homeostasis results from neutral

competition between symmetrically dividing Lgr5 stem cells. Cell *143*, 134–144.

Stern, C. (1936). Somatic Crossing over and Segregation in Drosophila Melanogaster. Genetics *21*, 625–730.

Subramanian, L., Calcagnotto, M.E., and Paredes, M.F. (2020). Cortical Malformations: Lessons in Human Brain Development. Front. Cell. Neurosci. *13*, 576.

Sun, Q., Lee, W., Mohri, Y., Takeo, M., Lim, C.H., Xu, X., Myung, P., Atit, R.P., Taketo, M.M., Moubarak, R.S., et al. (2019). A novel mouse model demonstrates that oncogenic melanocyte stem cells engender melanoma resembling human disease. Nat. Commun. *10*, 5023.

Supp, D.M., Witte, D.P., Potter, S.S., and Brueckner, M. (1997). Mutation of an axonemal dynein affects left-right asymmetry in inversus viscerum mice. Nature *389*, 963–966.

Takeo, Y.H., Shuster, S.A., Jiang, L., Hu, M.C., Luginbuhl, D.J., Rülicke, T., Contreras, X., Hippenmeyer, S., Wagner, M.J., Ganguli, S., and Luo, L. (2021). GluD2- and Cbln1-mediated competitive interactions shape the dendritic arbors of cerebellar Purkinje cells. Neuron *109*, 629–644.e8.

Tang, S.H., Silva, F.J., Tsark, W.M., and Mann, J.R. (2002). A Cre/loxP-deleter transgenic line in mouse strain 129S1/SvImJ. Genesis *32*, 199–202.

Tasic, B., Miyamichi, K., Hippenmeyer, S., Dani, V.S., Zeng, H., Joo, W., Zong, H., Chen-Tsai, Y., and Luo, L. (2012). Extensions of MADM (mosaic analysis with double markers) in mice. PLoS One *7*, e33332.

Taverna, E., Götz, M., and Huttner, W.B. (2014). The cell biology of neurogenesis: toward an understanding of the development and evolution of the neocortex. Annu. Rev. Cell Dev. Biol. *30*, 465–502.

Tian, A., Kang, B., Li, B., Qiu, B., Jiang, W., Shao, F., Gao, Q., Liu, R., Cai, C., Jing, R., et al. (2020). Oncogenic State and Cell Identity Combinatorially Dictate the Susceptibility of Cells within Glioma Development Hierarchy to IGF1R Targeting. Adv. Sci. (Weinh.) *7*, 2001724.

Tucci, V., Isles, A.R., Kelsey, G., and Ferguson-Smith, A.C.; Erice Imprinting Group (2019). Genomic Imprinting and Physiological Processes in Mammals. Cell *176*, 952–965.

Tuna, M., Knuutila, S., and Mills, G.B. (2009). Uniparental disomy in cancer. Trends Mol. Med. *15*, 120–128.

Van Keymeulen, A., Rocha, A.S., Ousset, M., Beck, B., Bouvencourt, G., Rock, J., Sharma, N., Dekoninck, S., and Blanpain, C. (2011). Distinct stem cells contribute to mammary gland development and maintenance. Nature *479*, 189–193.

Wuidart, A., Sifrim, A., Fioramonti, M., Matsumura, S., Brisebarre, A., Brown, D., Centonze, A., Dannau, A., Dubois, C., Van Keymeulen, A., et al. (2018). Early lineage segregation of multipotent embryonic mammary gland progenitors. Nat. Cell Biol. *20*, 666–676.

Xu, T., and Rubin, G.M. (1993). Analysis of genetic mosaics in developing and adult Drosophila tissues. Development *117*, 1223–1237.

Yadlapalli, S., and Yamashita, Y.M. (2013). Chromosome-specific nonrandom sister chromatid segregation during stem-cell division. Nature *498*, 251–254.

Yamashita, Y.M. (2013). Nonrandom sister chromatid segregation of sex chromosomes in Drosophila male germline stem cells. Chromosome Res. *21*, 243–254.

Yamazawa, K., Ogata, T., and Ferguson-Smith, A.C. (2010). Uniparental disomy and human disease: an overview. Am. J. Med. Genet. C. Semin. Med. Genet. *154C*, 329–334.

Yao, M., Ventura, P.B., Jiang, Y., Rodriguez, F.J., Wang, L., Perry, J.S.A., Yang, Y., Wahl, K., Crittenden, R.B., Bennett, M.L., et al. (2020). Astrocytic trans-Differentiation Completes a Multicellular Paracrine Feedback Loop Required for Medulloblastoma Tumor Growth. Cell *180*, 502–520.e19.

Yizhak, K., Aguet, F., Kim, J., Hess, J.M., Kübler, K., Grimsby, J., Frazer, R., Zhang, H., Haradhvala, N.J., Rosebrock, D., et al. (2019). RNA sequence analysis reveals macroscopic somatic clonal expansion across normal tissues. Science *364*, eaaw0726.

Yochem, J., and Herman, R.K. (2003). Investigating C. elegans development through mosaic analysis. Development *130*, 4761–4768.

Zong, H., Espinosa, J.S., Su, H.H., Muzumdar, M.D., and Luo, L. (2005). Mosaic analysis with double markers in mice. Cell *121*, 479–492.

Zugates, C.T., and Lee, T. (2004). Genetic mosaic analysis in the nervous system. Curr. Opin. Neurobiol. *14*, 647–653.

CellPress
OPEN ACCESS

STAR★METHODS

KEY RESOURCES TABLE

REAGENT or RESOURCE	SOURCE	IDENTIFIER
Antibodies		
Keratin 8 #ab59400	Abcam	RRID:AB_942041
Keratin 14 #PRB-155P	BioLegend (former Covance)	RRID:AB_292096
Beta-Catenin #8480	Cell Signaling	RRID:AB_11127855
Histone H3 phospho (Ser10) #3377	Cell Signaling	RRID:AB_1549592
CD3-HorizonV451	eBioscience	RRID:AB_1272193
CD19 APC	eBioscience	RRID:AB_469358
Fc Block CD16/32	BioLegend	RRID:AB_469358
Alexa Fluor 647 Anti-Rabbit IgG	Molecular Probes	RRID:AB_2762835
Anti-DIG AP	Merck	RRID:AB_2313640
Hoechst H33258	Sigma	No identifier
DAPI	Thermo-Fisher Scientific	No identifier
Chemicals, Peptides, and Recombinant Proteins		
ACK Lysis Buffer	Gibco	Cat#A1049201
DIG DNA Labelling Mix	Merck	11277065910
Blocking Reagent	Merck	Cat#11096176001
Positively Charged Nylon Membrane	Merck	Cat#11209272001
CDP-Star	Merck	Cat#11759051001
Horse Serum	Thermo-Fisher Scientific	Cat# 26050088
Triton X-100	Sigma-Aldrich	Cat#T878
GoTaq Master-Mix	Promega	Cat#M7123
TaKaRa PCR Amplification Kit	TaKaRa	Cat#R011A
TaKaRa TaqI Kit	TaKaRa	Cat#1189A
Nuclease-free Water	Thermo-Fisher Scientific	Cat#10977035
DABCO	Roth	Cat#0718.2
Mowiol	Roth	Cat#0713.2
Recombinant DNA		
MADM-1-GT targeting vector	This study	N/A
MADM-1-TG targeting vector	This study	N/A
MADM-2-GT targeting vector	This study	N/A
MADM-2-TG targeting vector	This study	N/A
MADM-3-GT targeting vector	This study	N/A
MADM-3-TG targeting vector	This study	N/A
MADM-4-GT targeting vector	This study	N/A
MADM-4-TG targeting vector	This study	N/A
MADM-5-GT targeting vector	This study	N/A
MADM-5-TG targeting vector	This study	N/A
MADM-6-GT targeting vector	This study	N/A
MADM-6-TG targeting vector	This study	N/A
MADM-8-GT targeting vector	This study	N/A
MADM-8-TG targeting vector	This study	N/A
MADM-9-GT targeting vector	This study	N/A
MADM-9-TG targeting vector	This study	N/A

(*Continued on next page*)

Continued

REAGENT or RESOURCE	SOURCE	IDENTIFIER
MADM-10-GT targeting vector	This study	N/A
MADM-10-TG targeting vector	This study	N/A
MADM-13-GT targeting vector	This study	N/A
MADM-13-TG targeting vector	This study	N/A
MADM-14-GT targeting vector	This study	N/A
MADM-14-TG targeting vector	This study	N/A
MADM-15-GT targeting vector	This study	N/A
MADM-15-TG targeting vector	This study	N/A
MADM-16-GT targeting vector	This study	N/A
MADM-16-TG targeting vector	This study	N/A
MADM-17-GT targeting vector	This study	N/A
MADM-17-TG targeting vector	This study	N/A
MADM-18-GT targeting vector	This study	N/A
MADM-18-TG targeting vector	This study	N/A
MADM-19-GT targeting vector	This study	N/A
MADM-19-TG targeting vector	This study	N/A
Oligonucleotides		
See Table S2		N/A
Experimental Models: Cell Lines		
Parental ES cell line C2, Stock Number: 011989-MU	A. Nagy	MMRRC_011989-MU
Experimental Models: Organisms/Strains/Lines		
Mouse: *MADM-1-GT*	This study	N/A
Mouse: *MADM-1-TG*	This study	N/A
Mouse: *MADM-2-GT*	This study	N/A
Mouse: *MADM-2-TG*	This study	N/A
Mouse: *MADM-3-GT*	This study	N/A
Mouse: *MADM-3-TG*	This study	N/A
Mouse: *MADM-4-GT*	This study	N/A
Mouse: *MADM-4-TG*	This study	N/A
Mouse: *MADM-5-GT*	This study	N/A
Mouse: *MADM-5-TG*	This study	N/A
Mouse: *MADM-6-GT*	This study	N/A
Mouse: *MADM-6-TG*	This study	N/A
Mouse: *MADM-7-GT*	The Jackson Laboratory	RRID:IMSR_JAX:021457
Mouse: *MADM-7-TG*	The Jackson Laboratory	RRID:IMSR_JAX:021458
Mouse: *MADM-8-GT*	This study	N/A
Mouse: *MADM-8-TG*	This study	N/A
Mouse: *MADM-9-GT*	This study	N/A
Mouse: *MADM-9-TG*	This study	N/A
Mouse: *MADM-10-GT*	This study	N/A
Mouse: *MADM-10-TG*	This study	N/A
Mouse: *MADM-11-GT*	The Jackson Laboratory	RRID:IMSR_JAX:013749
Mouse: *MADM-11-TG*	The Jackson Laboratory	RRID:IMSR_JAX:013751
Mouse: *MADM-12-GT*	The Jackson Laboratory	RRID:IMSR_JAX:021460
Mouse: *MADM-12-TG*	The Jackson Laboratory	RRID:IMSR_JAX:021461
Mouse: *MADM-13-GT*	This study	N/A
Mouse: *MADM-13-TG*	This study	N/A

(*Continued on next page*)

Continued

REAGENT or RESOURCE	SOURCE	IDENTIFIER
Mouse: *MADM-14-GT*	This study	N/A
Mouse: *MADM-14-TG*	This study	N/A
Mouse: *MADM-15-GT*	This study	N/A
Mouse: *MADM-15-TG*	This study	N/A
Mouse: *MADM-16-GT*	This study	N/A
Mouse: *MADM-16-TG*	This study	N/A
Mouse: *MADM-17-GT*	This study	N/A
Mouse: *MADM-17-TG*	This study	N/A
Mouse: *MADM-18-GT*	This study	N/A
Mouse: *MADM-18-TG*	This study	N/A
Mouse: *MADM-19-GT*	This study	N/A
Mouse: *MADM-19-TG*	This study	N/A
Mouse: *Emx1-Cre*	The Jackson Laboratory	RRID:IMSR_JAX:005628
Mouse: *Hprt-Cre*	The Jackson Laboratory	RRID:IMSR_JAX:004302
Mouse: *Nestin-Cre*	Petersen et al. 2002	N/A
Mouse: *Apc-flox*	The Jackson Laboratory	RRID:IMSR_JAX:009045
Mouse: *iv* mutant (*Dnah11 mutant*)	The Jackson Laboratory	RRID:IMSR_JAX:001045
Software and Algorithms		
ZEN Digital Imaging for Light Microscopy	Zeiss	http://www.zeiss.com/microscopy/en_us/products/microscope-software/zen.html#introduction
FACS Diva	BD Biosciences	N/A
Graphpad Prism 8.0	Graphpad	https://www.graphpad.com/scientific-software/prism/
FlowJo	Becton, Dickinson and Company; 2019	https://www.flowjo.com/
Photoshop	Adobe	adobe.com/products/photoshop
ImageJ		https://imagej.nih.gov/ij/
Other		
FACS Aria III	BD Biosciences	N/A
LSM 800 Confocal	Zeiss	N/A
SlideScanner VS120	Olympus	N/A
Cryostat Cryostar NX70	Thermo Fisher Scientific	N/A
Peqlab FUSION SL Advance	Peqlab	N/A

RESOURCE AVAILABILITY

Lead contact

Further information and requests for resources and reagents should be directed to and will be fulfilled by the Lead Contact, Simon Hippenmeyer (simon.hippenmeyer@ist.ac.at).

Materials availability

All published and inaugural reported reagents and mouse lines will be shared upon request within the limits of the respective material transfer agreements. All MADM lines will be made publicly available through *The European Mouse Mutant Archive* (EMMA) and distributed from the University of Veterinary Medicine in Vienna or the Institute of Science and Technology Austria in Klosterneuburg.

Data and code availability

This study did not generate code and all data have been presented in Figures and Supplemental Figures. Original images will be made available upon request.

EXPERIMENTAL MODEL AND SUBJECT DETAILS

Generation, breeding and husbandry of mouse lines

Experimental procedures were discussed and approved by the institutional ethics and animal welfare committees at IST Austria, Stanford University, and at University of Veterinary Medicine Vienna in accordance with good scientific practice guidelines and national legislation (license number: IST Austria: BMWF-66.018/0007-II/3b/2012 and BMWFW-66.018/0006-WF/V/3b/2017; University of Veterinary Medicine Vienna: BMWF-68.205/0023-II/3b/2014 and BMBWF-68.205/0010-V/3b/2019). Mice with specific pathogen free status according to FELASA recommendations (Mähler Convenor et al., 2014) were bred and maintained in experimental rodent facilities (room temperature 21 ± 1°C [mean ± SEM]; relative humidity 40%–55%; photoperiod 12L:12D). Food (V1126, Ssniff Spezialitäten GmbH, Soest, Germany) and tap water were available *ad libitum*.

Mouse lines with MADM cassettes inserted in Chr. 7 (Hippenmeyer et al., 2013), Chr. 11 (Hippenmeyer et al., 2010), and Chr. 12 (Hippenmeyer et al., 2013), *Emx1*-Cre (Gorski et al., 2003), *Nestin*-Cre (Petersen et al., 2002), *Hprt*-Cre (Tang et al., 2002), *Apc*-flox (Cheung et al., 2010), and *iv* mice [*Dnah11* mutation (Hummel and Chapman 1959)] have been described previously. *Nestin*-Cre mice were a kind gift from W. Zhong. Body weight and signs of anemia were evaluated for genetic mosaic *MADM-18*$^{GT/TG;Apc}$;*Hprt*$^{Cre/+}$ and corresponding MADM-18$^{GT/TG}$;*Hprt*$^{Cre/+}$ control mice once per week. All analyses were carried out in mixed genetic background. The two lines of each chromosome, with the exception of Chr. 7, 11 and 12, were designated as C57BL/6N;CD1-MADM-GT$^{tm1(Chr1)Biat}$ and C57BL/6N;CD1-MADM-TG$^{tm1(Chr1)Biat}$, as indicated here for Chr. 1. No sex specific differences were observed under any experimental conditions or in any genotype.

METHOD DETAILS

Molecular biology

Generation of MADM targeting constructs

Molecular cloning and generation of recombinant DNA to construct all plasmids (incl. targeting vectors, plasmids with southern probes etc.), and all nucleic acid procedures as described below were carried out according to standard cloning protocols (Sambrook et al., 1989).

Genomic DNA isolation from mouse ES cells

Mouse ES cells were lysed in Lysis Buffer (1M Tris-HCl pH = 7.5, 0.5M EDTA, 5M NaCl, 20% Sarcosyl, 20 mg/ml Proteinase K) overnight at 55°C. Next day, DNA was precipitated with isopropanol for 2 hr at room temperature with agitation and then carefully transferred into a fresh tube containing TE-buffer. The tubes were left open for 10 min to allow residual isopropanol to evaporate. DNA was then incubated for 3 hr at 37°C.

Southern blot

DIG-labeled probes were generated via PCR amplification of plasmid templates containing the probe sequence using a mix of nucleotides containing Digoxigenin-11-dUTP (DIG-dUTP). The PCR reaction was next separated by electrophoresis and the corresponding band was cut and gel purified using the Monarch DNA gel extraction Kit-NEB.

Genomic DNA was digested with the corresponding enzymes overnight at 37°C and electrophoresed in 0.8% agarose gels for 6 hr at low voltage together with Lambda Hind III marker. Next day, the agarose gels were depurinized in 0.25M HCl, denaturated in 0.4 NaOH and transferred overnight into a positively charged nylon membrane. Next day, agarose gels were assessed under UV light to verify complete transfer of DNA to the membrane. The nylon membrane was then neutralized in 0.5M Tris-HCl (pH = 7.5) and cross-linked with UV light. The membrane was incubated in hybridization buffer (5x SSC, 2% Blocking reagent, 50% Formamide, 0.1% Sarcosyl, 0.02% SDS) for 4 hr at 42°C in glass tubes in a rotating oven. In the meantime, the DIG-labeled probe was denaturated at 95°C for 10 min and then quickly chilled on ice for 5 min. The DIG-labeled probe in Hybridization buffer was added to the membrane and incubated overnight at 42°C in glass tubes in a rotating oven. Next day, stringency washes were performed with Wash Solution I (2xSSC, 0.1% SDS) at room temperature, followed by Wash Solution II (0.2x SSC, 0.1% SDS) at 68°C. Next day, the membrane was blocked in blocking solution (1% blocking reagent, 0.1M Maleic acid, 0.15M NaCl) for 1 hr. Then anti-DIG AP antibody (1:20,000) in Blocking Solution was added to the membrane, incubated for 30 min at room temperature and then washed with Wash buffer (0.1M Maleic acid, 0.15M NaCl, 0.3% Tween) for 15 min. Finally, the membrane was incubated with CDP-Star (1:100) chemiluminescent substrate in CDP-Star detection buffer (0.1M Tris-HCl, 0.1M NaCl, pH = 9.5) for 5 min, wrapped in transparent film and kept in the dark for 1 hr. The pattern of probe hybridization was detected in a Peqlab FUSION SL Advance system for chemiluminescent imaging.

Generation of transgenic MADM mice

Targeting of MADM constructs to mouse ES cells by electroporation

The linearized MADM targeting constructs were introduced into C57BL/6N embryonic stem cells (Parental ES cell line C2, Stock Number: 011989-MU, Citation ID: RRID: MMRRC_011989-MU, A. Nagy Basic ES Cell line) by electroporation using a Bio-Rad Gene Pulser Xcell. After selection with 150μg/ml G418, surviving clones were analyzed for correct targeted integration by Southern blot hybridization (see above). Metaphase spread chromosome counting was performed on ES cells of clones with confirmed correct targeting of the MADM cassettes before they were prepared for blastocyst injection.

Production of chimeras

Host blastocysts were produced by superovulation of BALB/cRj females by intraperitoneal (IP) injection with 5.0 IU of equine chorionic gonadotropin (Folligon; Intervet) and, 48 hr later, with 5.0 IU of human chorionic gonadotropin (Chorulon; Intervet) followed by mating with males of the same strain. Morula stages were harvested from isolated oviducts at day 2.5 days post coitum (dpc) and cultured in M16 medium overnight in an incubator at 37°C and 5% CO_2 to produce host blastocysts. About 10-15 ES cells were injected into a single blastocyst. The injected embryos were cultured for 2-3 hr to recover and then transferred into the right uterus horn of 2.5 dpc pseudopregnant RjOrl:Swiss surrogate mothers as described earlier in detail (Rülicke 2004, Rülicke et al., 2006). The offspring were selected based on their chimeric coat color. High-percentage male chimeras (> 80%) were bred with C57BL/6NRj females and the offspring were selected by coat color and genotyped by PCR for the respective GT or TG MADM transgenes.

Genotyping of MADM reporters, *Apc*-flox and *iv* mice

For primer sequences see Table S2. Forward and reverse primer 1 is specific for each MADM reporter. In the absence of MADM cassettes the forward/reverse primer 1 PCR will result in the WT band as indicated. The reverse primer 2 is generic and located in the MADM cassette. The forward/reverse primer 2 PCR will result in the MADM band as indicated. The combined use of all three (forward, reverse primer 1, and reverse primer 2) in a single PCR reaction will enable the distinction of WT (single band at WT size), heterozygote (two bands, one at WT and one at MADM size), and homozygous MADM (single band at MADM size) stock mice. Note that $MADM^{GT/GT}$ and $MADM^{TG/TG}$ stock mice should be maintained individually. The distinction of MADM-GT versus MADM-TG is possible by using GT-cassette (GT-for and GT-rev) and TG-cassette (TG for and TG rev) specific primers, respectively. Male mice can be identified by using Y chromosome (Ychrom for and Ychrom rev) specific primers. Presence of transgenes encoding Cre recombinase can be confirmed by using Cre primers (Cre for and Cre rev) as indicated.

Genotyping of *Apc*-flox mice was performed according to the protocol available at JAX. Genotyping of *iv* mice was performed using TaKaRa PCR Amplification Kit followed by a 16h enzymatic digestion using TaKaRa TaqI at 65°C. Separation of wt (50bp) and mutant (100bp) band was performed on a 6% agarose gel.

Isolation of MADM-labeled tissue

Mice were deeply anesthetized through injection of ketamine/xylazine/acepromazine solution (65 mg, 13 mg and 2 mg/kg body weight, respectively), and confirmed to be unresponsive through pinching the paw. Perfusion was performed with PBS followed by ice-cold 4% PFA. Tissue was further fixed in 4% PFA overnight at 4°C. Brain, thymus, heart, lung, liver, kidney, spleen, eye and spinal cord were surgically removed and cryopreserved in 30% sucrose for 48 hr and then embedded in Tissue-Tek O.C.T. (Sakura). All samples were stored at −20°C or −80°C until further usage. Samples were sectioned in a cryo microtome at a 10 μm (liver) or 45μm (all other samples) thickness. Brain samples were collected in 24 multi-well dishes and then mounted onto Superfrost Glass Slides (Thermo Fisher Scientific), all other samples were directly mounted on glass slides.

For isolation of skin, pancreas, mammary gland intestine and colon, no perfusion was required. Mice were sacrificed by cervical dislocation and back skin was prepared for histology as previously described (Amberg et al., 2015). Briefly, back skin was shaved and surgically removed above the spine and placed on lint-free surface. Abdominal mammary glands, pancreas and small intestines were surgically removed. Small intestines and colons were cut open longitudinally and made into Swiss rolls. All samples were incubated in 4% PFA at room temperature for 4hrs, then cryoprotected in 30% sucrose overnight at 4°C and embedded into Tissue-Tek O.C.T. (Sakura). All samples were stored at −20°C. Intestine samples from APC mice were sectioned at a 30μm thickness. All other samples were sectioned at a 20μm thickness and directly mounted onto Superfrost Glass Slides (Thermo Fisher Scientific).

Histology and immunostaining of MADM-labeled tissue

For immunofluorescence staining in skin, pancreas, mammary gland and intestine, sections were thawed at room temperature for 15 min and encircled with DAKO hydrophobic pen. Then, they were washed 3x for 5 min with PBS. Antigen retrieval was performed by adding pre-warmed citrate buffer pH = 6.0 to the samples and incubating them at 85°C for 30 min. Samples were washed 3x for 5 min with PBS, then incubated in blocking solution (10% horse serum, 0.5% Triton X-100 in PBS) for 1h at room temperature. Primary antibodies were diluted in staining solution (5% horse serum, 0.5% Triton X-100 in PBS) and added to the samples over night at 4°C. Next day, samples were washed 3x for 5min with PBS and incubated with secondary antibodies (1:1000) and Hoechst (Sigma, 1mg/ml stock, 1:1000) diluted in staining solution for 2hrs at room temperature. After washing 3x for 5min with PBS, samples were mounted with Mowiol and stored at 4°C until they were imaged at a Zeiss LSM800. Primary antibodies: Keratin 8 (Abcam, 1:100), Keratin 14 (BioLegend, 1:500), beta-Catenin (Cell Signaling, 1:100), phospho-H3(Ser10) (Cell Signaling, 1:800). Secondary antibody: donkey anti-rabbit Alexa647 (Molecular Probes). Mounted brain sections were washed 3x for 5 min in PBS, DAPI stained (1:20'000) for 10 min and then embedded in mounting medium containing 1,4-diazabicyclooctane (DABCO; Roth) and Mowiol (Roth).

Flow cytometry

Mice were sacrificed by cervical dislocation and spleens were collected in ice-cold PBS. Spleens were minced through a 70μm cell strainer. The strainers were then flushed with 10ml PBS-FBS (1x PBS, 2% FBS) and cell suspensions were centrifuged for 6min at 1,200rpm. Cell pellets were resuspended in 1ml ACK lysis buffer (GIBCO) and incubated for 30sec. Lysis reaction was stopped by

adding 10ml PBS-FBS. Cells were centrifuged for 6 min at 1,200 rpm. Pellets were resuspended in 1ml PBS-FBS and transferred to 5ml round-bottom FACS tubes via a 70μm cell strainer. Tubes were filled up with PBS-FBS and centrifuged for 6 min at 1,200 rpm. Cells were incubated with Fc block (BD Biosciences) for 5 min and then incubated with 100μl of antibody mastermix for 30min on ice. Antibodies CD3 HorizonV451 (eBioscience) and CD19 APC (eBioscience) were diluted 1:200. Finally, 4ml of PBS-FBS were added and cells were centrifuged for 6 min at 1,200 rpm. Flow cytometric sorting of GFP^+, tdT^+ and GFP^+ tdT^+ cells was performed on a BD AriaIII. Analysis was performed using FlowJo.

Analysis of MADM-labeled brains and peripheral tissue

Representative images were acquired at an inverted LSM800 or LSM880 confocal microscope (Zeiss) using 10X/20X objectives or 40X/63X oil objectives for acquisition of higher magnification images of immunostained tissue. Images where then processed using Zeiss Zen Blue software and Photoshop (Adobe). Images for quantification were acquired at an inverted LSM800 or LSM880 confocal microscope (Zeiss) or SlideScanner VS120 (Olympus) using 10X objective and processed via custom scripts in ImageJ. Tiled images, encompassing the entire region of interest were imported into Photoshop software (Adobe) and the boundaries for the region of interest were traced. MADM-labeled cells were manually counted based on respective marker expression.

Adenomas in *MADM-18*$^{GT/TG;Apc}$;*Hprt*$^{Cre/+}$ mice intestine or colon were classified based on pathological criteria described previously (Behrens et al., 1998; Fodde et al., 2001; Barker et al., 2009) such as nucleic dysplasia (enlarged and elongated nuclei, strong nuclear staining), invasion of adenomatous epithelium into the lamina propria and up into the villus, coverage of adenomatous epithelium by a normal surface mucosa, polypoid lesion morphology with depressed center, mitotic figures within the adenomatous epithelium.

QUANTIFICATION AND STATISTICAL ANALYSIS

See Table S3 for complete information regarding quantifications and statistics used in this study. Table S3 includes all graphed values, including SEMs, p values, and exact values of n. Statistical analysis was performed in the software Prism8 (GraphPad). Evaluation of data was performed by the Welch's unequal variances t test (Figures 4, 5B, 6A, and 6D), Welch's ANOVA (Figures 5E, 6C, and 6D) or two-way ANOVA (Figure 6C). Data expressed as ratio was log-transformed prior to the statistical test. For Figures 4 and 5B, n was defined as the density of green/red cells per mm^3 from one animal resulting from the quantification of 4-20 sections. For Figures 5 and 6, n was defined as the YGR index for one animal resulting from the quantification of 10-24 sections (Figures 5E, 6A, and 6C), or from FAC-sorted cells from one animal (Figure 6D). The YGRI was defined as the ratio of yellow cells divided by the average of green and red cells.